

Spectral variation across Pulsar Profile due to Coherent Curvature Radiation

RAHUL BASU,^{1,2} DIPANJAN MITRA,^{3,1} AND GEORGE I. MELIKIDZE^{1,4}

¹*Janusz Gil Institute of Astronomy, University of Zielona Góra, ul. Szafrana 2, 65-516 Zielona Góra, Poland.*

²*Inter-University Centre for Astronomy and Astrophysics, Pune, 411007, India.*

³*National Centre for Radio Astrophysics, Tata Institute of Fundamental Research, Pune 411007, India.*

⁴*Evgeni Kharadze Georgian National Astrophysical Observatory, 0301 Abastumani, Georgia.*

Submitted to The Astrophysical Journal

ABSTRACT

The pulsar profile is characterised by two distinct emission components, the core and the cone. The standard model of a pulsar radio emission beam originating from dipolar magnetic fields, places the core at the centre surrounded by concentric layers of inner and outer conal components. The core emission is expected to have steeper spectra compared to the cones. We present a detailed analysis of the relative differences in spectra between the core and conal emission from a large sample of 53 pulsars over a wide frequency range between 100 MHz and 10 GHz. The core was seen to be much steeper than the cones particularly between 100 MHz and 1 GHz with a relative difference between the spectral index $\Delta\alpha_{core/cone} \sim -1.0$. In addition we also found the spectra of the outer conal components to be steeper than the inner cone with relative difference in the spectral index $\Delta\alpha_{in/out} \sim +0.5$. The flattening of the spectra from the magnetic axis towards the edge of the open field line region with increasing curvature of the field lines is a natural outcome of the coherent curvature radiation from charged soliton bunches, and explains the difference in spectra between the core and the cones. In addition due to the relativistic beaming effect, the radiation is only visible when it is directed towards the observer over a narrow angle $\theta \leq 1/\gamma$, where γ is the Lorentz factor of the outflowing plasma clouds. This restricts the emission particularly from outer cones, that are associated with field lines with larger curvature thereby making the spectra steeper than the inner cones.

Keywords: pulsars:

1. INTRODUCTION

The radio emission from normal period pulsars ($P > 0.1$ second) with measured flux density over a wide frequency range, between 100 MHz and 10 GHz, exhibit a inherently steep power law spectra with typical spectral index, $\alpha \sim -1.8$ ($S \propto \nu^\alpha$, Lorimer et al. 1995; Maron et al. 2000; Jankowski et al. 2018). In most cases the spectral index is obtained from the total flux density estimated across the average pulse profile. The pulsar profiles have complex shapes, usually comprising of several Gaussian like components, and detailed phenomenological studies suggest that the components have specific locations within the pulse window. The pulsar radio emission beam has a roughly circular shape, and can be described by the so called ‘core-cone’ model. According to this model the beam consists of a central core surrounded by two rings of nested conal emission, namely the inner and the outer cones (Rankin 1990, 1993; Mitra & Deshpande 1999). The width and shape of the pulse profile depends on the pulsar geometry and observers’ line of sight (LOS) traverse across the emission beam. Central LOS cuts form core-cone Triple (T) and core-double cone multiple (M) profile types, while the profile shape becomes conal Quadruple (${}_c$ Q), conal Triple (${}_c$ T) and double (D) shaped as the LOS traverses are progressively away from the magnetic axis. $T_{1/2}$ is another form of core-cone profile with two components where a conal component on one side of the core is either missing or too weak to detect at certain frequencies. A core single (S_t) profile signifies a central LOS traverse where the conal components are absent while a conal single (S_d) profile corresponds to peripheral LOS cuts. Table 1 summarises the classification scheme of the pulsar profile types. It has also been shown that the distribution of both the core and the conal component widths with period has similar lower boundary lines which is proportional to $P^{-0.5}$ (Maciesiak et al. 2012; Skrzypczak et al. 2018),

Table 1. Summary of Profile Classification

Symbol	Type	No. of Components	LOS Cut of Emission Beam
S_d	Cone	1	Outer Edge
S_t	Core	1	Center
D	Cone	2	Closer to the outer Edge
$T_{1/2}$	Core-Cone	2	Center
${}_cT$	Cone	3	Middle
T	Core-Cone	3	Center
${}_cQ$	Cone	4	Closer to the Center
M	Core-Cone	5	Center

suggesting similar emission heights for both. The pulsar emission is usually highly polarized and shows a polarization position angle (PPA) swing across the profile that resemble a S-shape curve. This is a result of the emission originating from strictly dipolar magnetic field region (Rotating Vector Model, Radhakrishnan & Cooke 1969). One of the most significant details about the origin of radio emission comes from constrains on its location at heights of 100-1000 km from the stellar surface. These are obtained from two independent estimates, the geometrical morphology described above (Rankin 1993; Kijak & Gil 1998; Mitra & Rankin 2002; Kijak & Gil 2003) and the aberration-retardation effect that shifts the PPA from the profile center, with the displacement being proportional to the emission height (Blaskiewicz et al. 1991; Phillips 1992; Xilouris et al. 1996; Mitra & Li 2004; Weltevrede & Johnston 2008; Krzeszowski et al. 2009).

Once it is established that the emission arises from a narrow range of heights in the dipolar magnetic field region, a gradual variation in certain emission properties is also expected due to change in curvature, from the central field lines near the axis towards the edge of the open field line region. This is reflected in the PPA particularly in the central LOS traverses where the core component is associated with large PPA variations, while the PPA traverse is relatively flat across the cones (Rankin 1990, 1993). Apart from having specific location within the pulsar beam, the core and conal flux densities exhibit different spectra, with the core emission having a steeper spectra compared to the cones (Rankin 1983). This effect is once again best observed in T and M profiles, when the core, inner and outer cones are clearly visible across different frequencies. However, it is more complicated to measure the flux densities from pulsars as they require detailed instrumental calibration for scaling the flux level of the measured signal. The pulsar emission also shows variability due to scintillation in the intervening medium (Rickett 1990), and hence it is essential to average over multiple observing sessions to find a mean level. A way around the issues with flux measurement has been suggested in the recent work of Basu et al. (2021), where it was noted that the different components in the profile are equally affected by the flux scaling and scintillation issues and hence the ratio between their intensities is unaffected by these variations. The frequency evolution of the ratio between the components can be used to find the difference in spectra between the core and the different types of conal emission. The spectral difference between the core and the conal emission in 21 pulsars observed in the MSPES survey at 325 and 610 MHz (Mitra et al. 2016) were estimated and the core was found to be steeper than the cone with $\Delta\alpha_{core/cone} \sim -0.7$. In addition it was also found that the inner cone was less steep compared to the outer cones where $\Delta\alpha_{in/out} \sim +0.3$.

Currently there are no physical models that can explain why the pulsar spectra varies across the emission beam? On the other hand several observational features in pulsars like the radio emission heights, polarization properties, etc., suggest that the pulsar emission can be excited by curvature radiation from charge bunches in a relativistically flowing electron-positron plasma (Ruderman & Sutherland 1975; Melikidze et al. 2000; Gil et al. 2004; Mitra et al. 2009; Melikidze et al. 2014; Mitra 2017). These charge bunches are formed due to nonlinear growth of plasma instability that leads to formation of relativistic, charged solitons (Gil et al. 2004; Melikidze et al. 2014; Lakoba et al. 2018; Rahaman et al. 2020). Melikidze et al. (2000) also showed that there are significant differences between the spectrum of a single particle curvature radiation and a charge bunch of finite length. Thus using the constraints from observations and the

theory of coherent curvature radiation it is now possible to address the origin of pulsar spectral index and its variation across different components.

In this paper we aim to carry out an exhaustive study of the spectra of the pulsar profile. A large number of average profiles in a wide frequency range has been measured and made publicly available over many decades of pulsar studies (Lorimer et al. 1995; Seiradakis et al. 1995; von Hoensbroech & Xilouris 1997; Kijak et al. 1998; Gould & Lyne 1998; Weisberg et al. 1999; Bilous et al. 2016; Mitra et al. 2016; Johnston & Kerr 2018). We have estimated the spectral variations of the different component types in 53 pulsars, from archival profiles over a wide frequency range, between 100 MHz and 10 GHz. We also explore the variations expected in the spectra across the emission beam due to curvature radiation from charge bunches and compare with the measurements.

2. AVERAGE PROFILE ANALYSIS

The primary analysis concerns with estimating the relative differences in spectra between different component types, core, inner cone and outer cones, within the pulsar average profile. Following the suggestion of Basu et al. (2021), the spectral difference between between different component types is estimated as :

$$\begin{aligned}
 S_{core} &= S_1 \nu^{\alpha_{core}} \\
 S_{cone} &= S_2 \nu^{\alpha_{cone}} \\
 S_{in} &= S_3 \nu^{\alpha_{in}} \\
 S_{out} &= S_4 \nu^{\alpha_{out}} \\
 \left(\frac{S_{core}}{S_{cone}}\right) &= \left(\frac{S_1}{S_2}\right) \nu^{\Delta\alpha_{core/cone}} \quad \Delta\alpha_{core/cone} = \alpha_{core} - \alpha_{cone} \\
 \left(\frac{S_{core}}{S_{in}}\right) &= \left(\frac{S_1}{S_3}\right) \nu^{\Delta\alpha_{core/in}} \quad \Delta\alpha_{core/in} = \alpha_{core} - \alpha_{in} \\
 \left(\frac{S_{core}}{S_{out}}\right) &= \left(\frac{S_1}{S_4}\right) \nu^{\Delta\alpha_{core/out}} \quad \Delta\alpha_{core/out} = \alpha_{core} - \alpha_{out} \\
 \left(\frac{S_{in}}{S_{out}}\right) &= \left(\frac{S_3}{S_4}\right) \nu^{\Delta\alpha_{in/out}} \quad \Delta\alpha_{in/out} = \alpha_{in} - \alpha_{out}
 \end{aligned} \tag{1}$$

It is expected that any variations due to scintillation or lack of flux calibration will affect all components of the profile in an identical manner and hence any properly formed average profile is useful for the spectral difference studies. However, the pulsar need to have different component types and these studies are viable in core-cone profiles, T and M, and conal profiles with clearly distinguished inner and outer cones, ${}_c$ Q and ${}_c$ T. Profile classification studies were initiated in the pioneering works of Rankin (1990, 1993) and has been expanded in recent years (Mitra & Rankin 2011; Basu et al. 2019; Olszanski et al. 2019). We found around 150 pulsars in the literature that were classified as one of the four relevant profile types. The spectra studies can be carried out only if profile measurements are available at two or more well separated frequency bands with sufficient temporal resolution to detect the individual components. The emission components also show frequency evolution due to various effects like radius to frequency mapping, LOS evolution with frequency, relative spectral difference between components (the topic of our study), etc., such that in many pulsars one or more components either merge together or vanish at certain frequencies. This left us with 53 pulsars, where profiles with distinct component types are available at more than one frequency.

Table 2 shows details of the 53 pulsars used for the spectra studies. The list consists primarily of T and $T_{1/2}$ profiles and include 43 such pulsars, while another 6 are of M type and 4 have ${}_c$ T/ ${}_c$ Q profiles. The frequency coverage is wide, ranging from around 100 MHz up to 10 GHz in a few cases, with around 40 percent (21 pulsars) of the sample having measurements at more than three different frequencies. The Table also reports the average spectral index for each pulsar, the sample showing typical steep spectra behaviour with values ranging mostly between -1.0 and -2.5. The presence of the core component in most of the profiles also allowed us to estimate the magnetic inclination angle (ϑ), where the 50% width of the core (W_{50}) at 1 GHz can be associated with emission geometry as $W_{50} = 2.45P^{-0.5}/\sin\vartheta$ (Rankin 1990). We also list the frequency range over which average profile measurements were available in each pulsar as well as the total number of such measurements (Nfreq).

In Fig.1 two examples of the frequency evolution of the profile components are shown. The left panel corresponds to the M type pulsar B1237+25 with four profiles at 180 MHz, 325 MHz, 610 MHz and 1400 MHz, while the right

Table 2. Pulsar List

	PSR	Period	Class	Spectral Index	Incl. angle	Freq. Range	Nfreq	Method
		(s)			($^{\circ}$)	(MHz)		
1	B0203-40	0.631	$T_{1/2}$	—	72	325 – 1400	2	Peak
2	B0329+54	0.715	T	-1.6	30	140 – 4850	9	Total
3	B0450+55	0.341	T	-1.2	32	325 – 4850	7	Avg
4	B0621-04	1.039	M	-1.0	32	410 – 1408	3	Peak
5	B0626+24	0.477	$T_{1/2}$	-1.5	30	170 – 4850	4	Peak
6	B0844-35	1.116	cQ	-2.0	26	325 – 610	2	Avg
7	B0919+06	0.431	T	-1.8	48	135 – 610	3	Avg
8	B0940-55	0.664	T	-2.6	34	1400 – 3100	2	Total
9	J1034-3224	1.151	cQ	-1.6	20	325 – 1400	4	Total
10	B1046-58	0.124	cT	-0.5	—	1400 – 8356	2	Total
11	J1141-3322	0.291	T	-1.2	36	436 – 1400	2	Total
12	B1154-62	0.401	T	-2.4	17	1400 – 3100	2	Total
13	B1237+25	1.382	M	-1.8	53	120 – 1400	5	Avg
14	B1323-58	0.478	$T_{1/2}$	-1.8	52	1400 – 8356	3	Peak
15	B1325-49	1.479	M	—	~ 90	325 – 610	2	Total
16	B1353-62	0.456	T	-1.8	27	1400 – 3100	2	Total
17	B1508+55	0.740	T	-2.3	45	140 – 325	3	Total
18	B1541+09	0.748	T	-2.1	5	140 – 1418	5	Avg
19	J1557-4258	0.329	T	—	67	610 – 1400	2	Total
20	B1556-44	0.257	T	-2.3	32	325 – 1560	3	Peak
21	B1600-49	0.327	T	-1.6	~ 90	610 – 1400	2	Total
22	J1625-4048	2.355	T	—	29	436 – 1400	3	Total
23	B1642-03	0.388	T	-2.3	70	610 – 10550	5	Avg
24	B1700-32	1.212	T	-1.5	48	325 – 610	2	Total
25	B1732-07	0.419	T	-1.8	64	325 – 1400	3	Avg
26	B1737+13	0.803	M	-1.4	41	325 – 1418	5	Total
27	B1738-08	2.043	cQ	-2.5	26	325 – 610	2	Avg
28	B1758-29	1.082	T	-2.0	36	325 – 1400	3	Total
29	B1804-08	0.164	T	-1.4	63	610 – 3100	4	Total
30	B1821+05	0.753	T	-1.7	32	325 – 4850	7	Total
31	B1826-17	0.307	T	-1.7	39	925 – 1408	2	Total
32	B1831-03	0.687	T	-2.8	54	925 – 1400	2	Peak
33	B1831-04	0.290	M	-1.3	10	325 – 610	2	Avg
34	B1839+09	0.381	T	-2.0	83	130 – 4850	4	Peak
35	B1857-26	0.612	M	-1.2	25	325 – 1400	5	Total
36	B1859+03	0.655	$T_{1/2}$	-2.7	35	925 – 1642	3	Peak
37	B1907+00	1.017	T	-1.8	69	610 – 1418	2	Total
38	B1907+10	0.284	$T_{1/2}$	-1.9	49	610 – 1400	2	Peak
39	B1907-03	0.505	T	-2.6	33	610 – 1420	2	Avg
40	B1911+13	0.521	T	-1.4	52	606 – 1418	2	Peak
41	B1914+09	0.270	$T_{1/2}$	-2.3	52	325 – 1642	6	Total
42	B1917+00	1.272	T	-2.3	81	325 – 1642	5	Total
43	B1918+26	0.786	$T_{1/2}$	-1.3	44	170 – 1418	2	Peak
44	B1920+21	1.078	$T_{1/2}$	-2.4	44	610 – 1642	4	Peak
45	B1929+10m	0.227	T	-1.7	~ 90	120 – 10550	10	Peak
46	B1946+35	0.717	T	-2.2	34	925 – 4850	4	Peak
47	B1952+29	0.427	T	—	30	610 – 1418	2	Peak
48	B2002+31	2.111	T	-1.5	49	610 – 1642	3	Total
49	B2045-16	1.962	T	-1.7	36	325 – 4850	7	Total
50	B2111+46	1.015	T	-2.0	9	408 – 4850	7	Total
51	B2210+29	1.005	T	-1.4	41	130 – 1418	4	Total
52	B2224+65	0.683	$T_{1/2}$	-1.7	16	325 – 1642	7	Peak
53	B2327-20	1.644	T	-2.1	60	325 – 610	2	Total

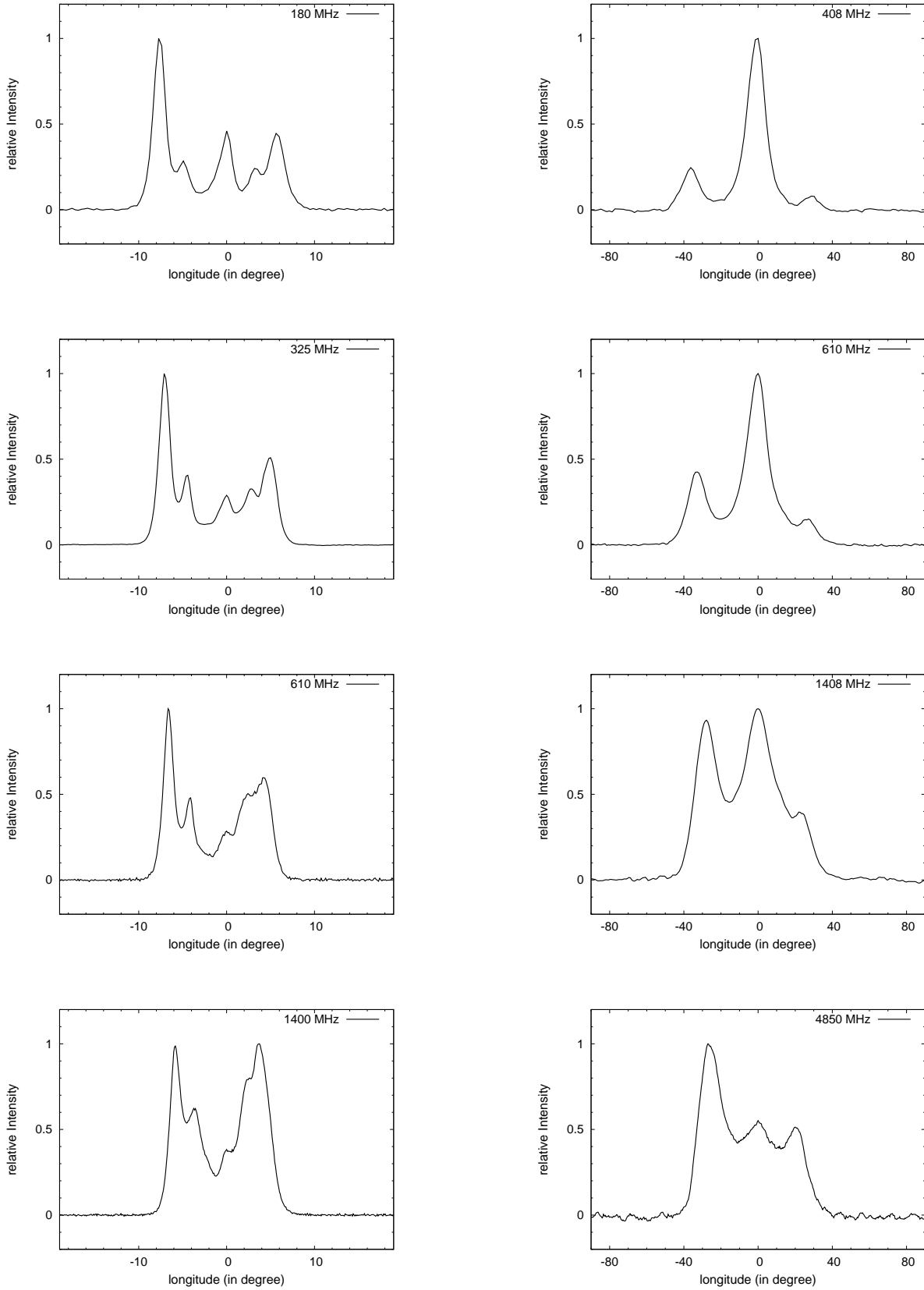


Figure 1. The figure shows evolution of the average profile over four different frequency bands in two different pulsars, B1237+25 (left panel) with M type profile and B2111+46 (right panel) with T profile type. The references for each measurement is listed in Table 3.

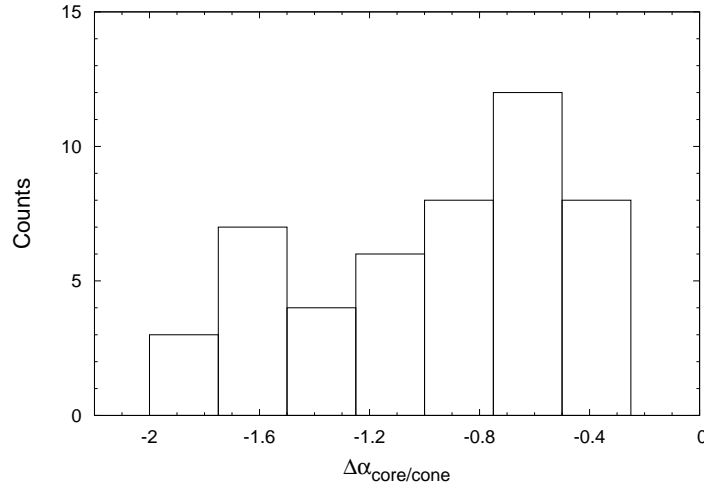


Figure 2. The distribution of the spectral difference between the core and conal components.

panel shows the T type pulsar B2111+46 at 408 MHz, 610 MHz, 1408 MHz and 4850 MHz. In both cases the central core component has higher relative intensities at the lower frequencies compared to the cones. It is apparent from the figure that the different component types show significant evolution with frequency and in many cases the components merge together at one or more frequencies (see core emission at 1400 MHz for B1237+25). Hence, it becomes difficult to estimate the total power in the components for the spectra calculations at certain frequencies, and the peak or the average intensities in the components provide better estimates in such cases. The last column in Table 2 lists the method by which the intensities of the components were estimated in each pulsar. The peak intensities are estimated from Gaussian approximation of suitably selected points around the expected peak. In instances where the average intensities are used, the adjacent components are not clearly separated. The longitude corresponding to the minimum intensity between these components is considered the boundary for the measurements. The intensity ratio between the components is used to estimate the relative spectra. As a result no additional scaling is required when using the peak or the average intensities since they are expected to affect both components in a similar manner.

3. RELATIVE SPECTRAL DIFFERENCE MEASUREMENTS

We have measured the ratio of the intensities between the core and the cone (S_{core}/S_{cone}) in 49 pulsars, the core and inner and outer cones, (S_{core}/S_{in} and S_{core}/S_{out}) in 5 pulsars, and between the inner and outer cones (S_{in}/S_{out}) in 9 pulsars, from profiles in different frequencies. These measurements are reported in Table 3 as well as the difference in the spectral index between the different component types and the frequency range over which the spectra is calculated. The spectral difference between the core and conal components ($\Delta\alpha_{core/cone}$) shows a relatively wide spread between -0.2 and -2.0 with a fairly uniform distribution as shown in Fig.2. A slight peak around $\Delta\alpha_{core/cone} \sim -0.7$ is visible which is consistent with earlier results (Basu et al. 2021). No clear correlation is seen between $\Delta\alpha_{core/cone}$ and different physical parameters like period, characteristic age, spin-down energy loss and the average spectral index. The spectral difference between the inner and outer cones ($\Delta\alpha_{in/out}$) in 9 pulsars varies between +0.1 and +0.8 with a mean value of +0.4. The spectra variation of the relative intensities of different components of 19 pulsars where measurements were available over relatively wide frequency range are shown in Fig. 3, 4, 5. We briefly discuss below the profile characteristics and component frequency evolution in all these cases.

B0329+54 : The pulsar profile has three distinct components with a bright core and has been classified as a T type profile (Rankin 1993). The pulsar is very bright with average flux density >200 mJy at 1 GHz (Lorimer et al. 1995) and has been observed over a wide frequency range from 40 MHz to around 30 GHz. The core component is asymmetrical with elongation near the leading edge. The pulsar emission is scattered and the components indistinguishable at frequencies below 100 MHz while one or more components vanish at the high frequency range above 10 GHz. The components also exhibit radius to frequency mapping with the two conal components being well separated from the core at lower frequencies, while the components merge at frequencies above 1 GHz but are still distinguishable up to 10 GHz. S_{core}/S_{cone} shows a power law frequency dependence between 400 MHz and 2 GHz (see Fig. 3, first row,

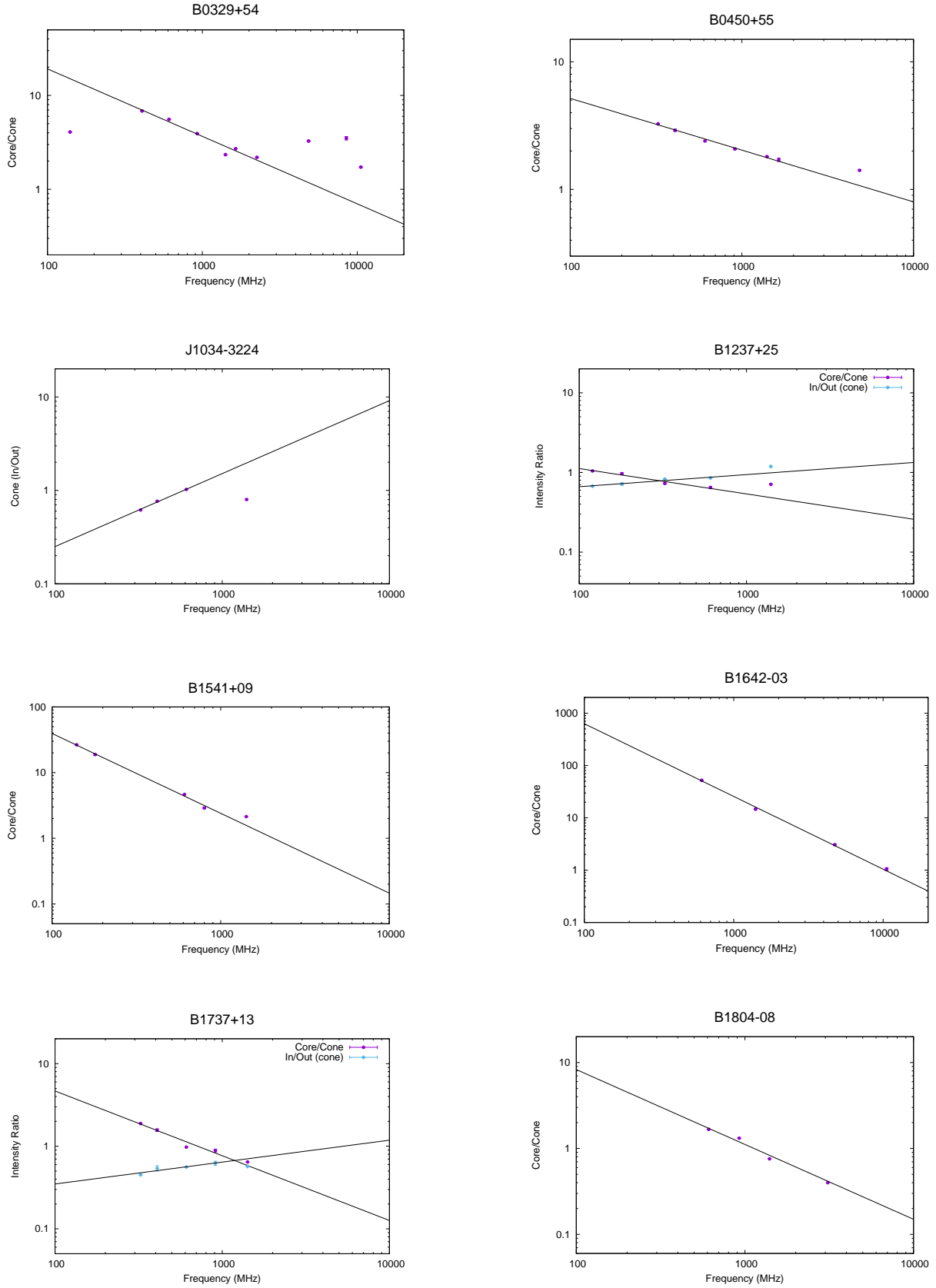


Figure 3. The figure shows the spectra of the relative intensities between the core and conal components within the pulsar profile in 8 pulsars between 100 MHz and 10 GHz. The spectral evolution between the inner and outer cones are also estimated in PSR B1237+25 and B1737+13 with M profile type as well as PSR J1034-3224 with cQ profile.

left panel) with $\Delta\alpha_{core/cone} \sim -0.7$. The spectral difference are flatter at lower frequencies while at the high frequency end the relative intensities become more irregular.

B0450+55 : The pulsar has an asymmetric profile with three merged components with trailing component showing a prominent tail. The profile was classified as T type and is part of the partial cone sample (Mitra & Rankin 2011). The leading component component is not distinguishable from the core at frequencies below 300 MHz and as result these profiles not used. Due to the components being merged together the average intensities are used to estimated the evolution of the relative spectra between the components which show a power law dependence between 300 MHz and 4.8 GHz with $\Delta\alpha_{core/cone} \sim -0.4$ (see Fig. 3, first row, right panel).

J1034-3224 : The pulsed emission is relatively wide occupying around 30 percent of the profile window and can be classified into two distinct parts the main pulse and a precursor component (Basu & Mitra 2018). The precursor becomes more prominent at higher frequencies (> 1 GHz) and is characterised by large fractional linear polarization and flat PPA traverse across the component (Basu et al. 2015). The main pulse consists of four distinct conal components and is classified as a c Q profile type. The pulsar was observed between 300 MHz and 1.4 GHz and the main pulse shows distinct evolution over this range. A large plateau is seen between the inner conal components at 325 MHz. The separation between the inner cones narrows with frequency and at 1.4 GHz the two components merge. The intensity of the outer cones increases in comparison with the inner cones with decreasing frequency and has a relative difference in spectral index below 1 GHz as $\Delta\alpha_{in/out} \sim +0.78$ (see Fig. 3, second row, left panel). The 1.4 GHz measurements is not used for the relative spectral index estimate.

B1237+25 : The central core in this M type profile is relatively weak and is clearly visible only at frequencies of 325 MHz and below (see Fig. 1). The spectra of the relative intensities between the core and the cones show a power law dependence below 1 GHz (see Fig. 3, second row, right panel), while at higher frequencies the measurements become less clear due to the core merging with the inner cone and the conal components overlapping each other. As a result only the leading side of the core is used to estimate the relative intensities at all frequencies. In this pulsar the spectral differences are relatively flat with $\Delta\alpha_{core/cone} \sim -0.3$ while $\Delta\alpha_{in/out} \sim +0.15$, which are near the upper and lower ends of the distributions, respectively.

B1541+09 : The pulsar has a wide profile which encompasses almost half the rotation period and has a T type classification. The conal emission is very low at lower frequencies from 400 MHz and below, but becomes more prominent at higher frequencies. The relative intensities show a power law spectra from 100 MHz to 1.4 GHz with relatively steep spectral difference $\Delta\alpha_{core/cone} \sim -1.2$ (see fig. 3, third row, left panel).

B1642-03 : The pulsar is classified as T type profile with a prominent core emission and has measurements over a wide frequency range between 100 MHz and 10 GHz. However, the conal emission is relatively weak and undetectable at frequencies below 600 MHz. At higher frequencies the conal emission merges with the core without clear boundaries between them and hence the average intensities are used for estimating the relative spectra evolution. The estimated spectra between 610 MHz and 10 GHz is $\Delta\alpha_{core/cone} \sim -1.4$ (see Fig. 3, third row, right panel).

B1737+13 : The pulsar profile has a prominent core emission with the profile classified as M type. However, the pulsar profile is asymmetric with only one conal component seen in the trailing side for most of the observing frequencies. The core emission shows a steeper spectra compared to the cone with the relative intensities showing a power law nature between 325 MHz and 1.4 GHz with $\Delta\alpha_{core/cone} \sim -0.8$ (see Fig. 3, fourth row, left panel). The outer cones also exhibit a steeper spectra compared to the inner cone with $\Delta\alpha_{in/out} \sim +0.3$.

B1804-08 : The pulsar has a T type profile with multiple reported measurements between 400 MHz and 5 GHz. At lower frequencies less than 900 MHz the components are merged together and cannot be measured separately. Between 900 MHz and 3 GHz the relative intensities show a power law spectra (see Fig. 3, fourth row, right panel) with $\Delta\alpha_{core/cone} \sim -0.9$. The components are once again indistinguishable in 5 GHz profile.

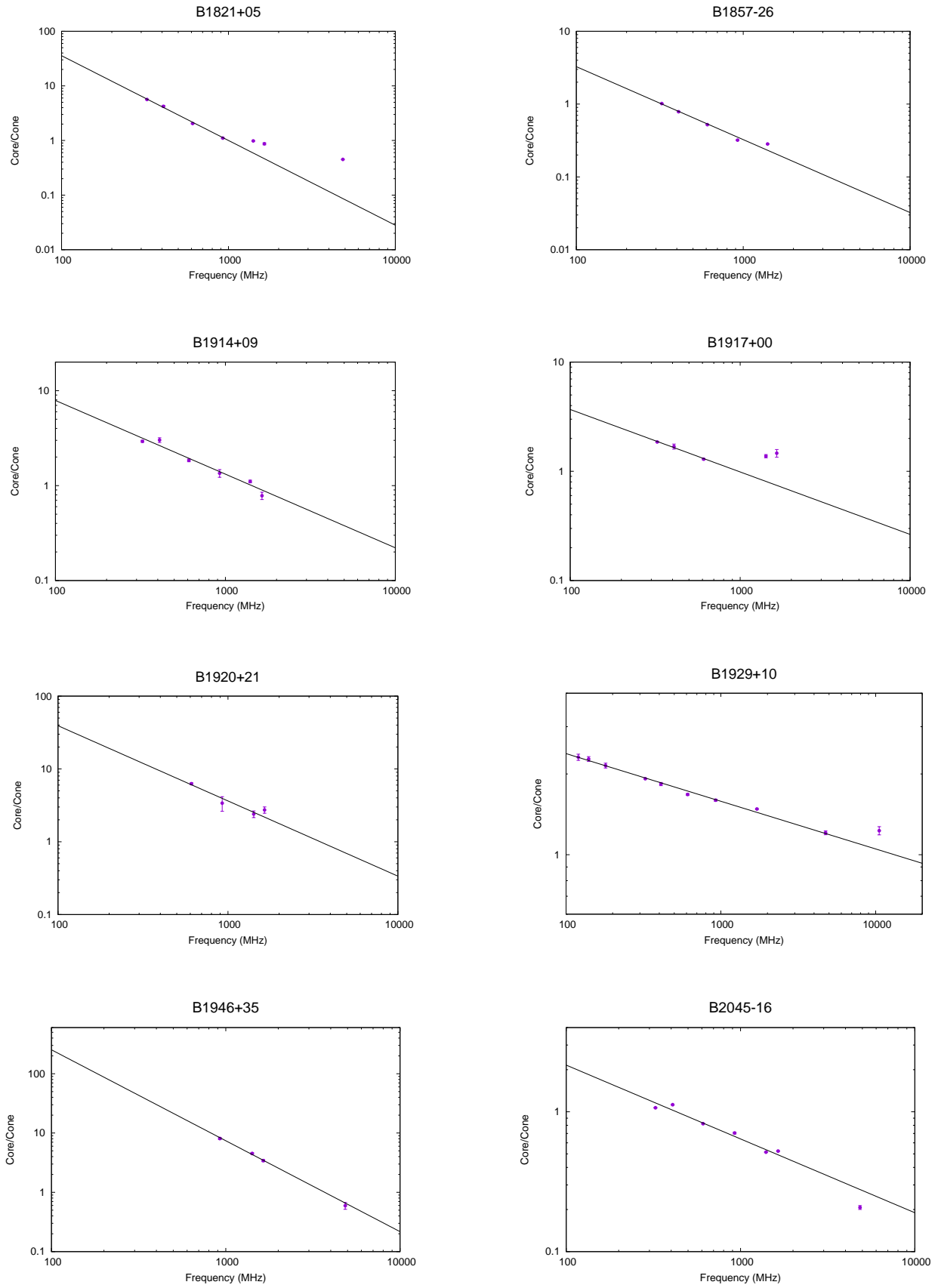


Figure 4. The figure shows the spectra of the relative intensities between the core and conal components within the pulsar profile in additional 8 other pulsars between 100 MHz and 10 GHz.

B1821+05 : The pulsar also has a T profile type with measurements available from 100 MHz to 5 GHz. The conal emission is not seen around 100 MHz while at frequencies above 1 GHz the core merges with the trailing cone. The relative intensities between the core and conal components show a power law spectra between 300 MHz and 1 GHz with spectral index $\Delta\alpha_{core/cone} \sim -1.55$ (see Fig. 4, first row, left column). The spectra becomes flatter at the higher frequency range likely due to mixing of component intensities. As a result the measurements at 1.4 GHz, 1.6 GHz and 4.8 GHz are not used for the relative spectral index estimate.

B1857-26 : This pulsar with M type profile shows prominent core as well as pairs of inner and outer cones between 300 MHz and 1 GHz. The components merge together at higher frequencies, and although it is still possible to distinguish the core at 1.4 GHz, the inner and outer cones merge together and cannot be measured separately. The evolution of the spectra of relative intensity between the core and the cones can be constrained using a power law nature between 300 MHz and 1.4 GHz with $\Delta\alpha_{core/cone} \sim -1.0$ (see Fig. 4, first row, right column). The outer cone has a steeper spectra than the inner cone between 300 MHz and 1 GHz with $\Delta\alpha_{in/out} \sim +0.35$.

B1914+09 : The pulsar has two components in the profile with the leading component being the core and the trailing component the cone, and classified as $T_{1/2}$. The components merge together and cannot be distinguished at frequencies around 100 MHz and 5 GHz. In the intervening frequency range of 325 MHz and 1.4 GHz the relative intensity of the core and the conal components shows a power law spectral dependence with $\Delta\alpha_{core/cone} \sim -0.8$ (see Fig. 4, second row, left column).

B1917+00 : The pulsar is characterised by a T type profile with the conal components not clearly separated from the core. In many profiles the time resolutions are insufficient to resolve the components. The relative intensity between the core and the cone show a power law dependence between 325 MHz and 610 MHz which flattens at 1.4 GHz (see Fig. 4, second row, right column). The estimated $\Delta\alpha_{core/cone}$ between 325 and 610 MHz is around -0.6. The high frequency measurements at 1.4 GHz and 1.6 GHz are not used for the relative spectral index estimate.

B1920+21 : The pulsar has a $T_{1/2}$ profile with a prominent core emission along with a trailing conal component. At frequencies around 100 MHz the profile is affected by scattering. Below 600 MHz the conal emission is very weak and cannot be clearly measured, while between 600 MHz and 1.6 GHz the relative intensities between the core and the cone has a power law spectral nature with $\Delta\alpha_{core/cone} \sim -1.0$ (Fig. 4, third row, left column).

B1929+10 : The pulsar has a diverse profile where in addition to the main pulse an interpulse emission is seen approximately 180° away in phase. There is also the presence of a wide postcursor component between the main pulse and the interpulse (Rankin & Rathnasree 1997; Basu et al. 2015; Kou et al. 2021). The main pulse also shows high levels of linear polarization with almost 100 percent fractional polarization and hence is often used to calibrate the polarization response in Telescopes (Mitra et al. 2016). As a result the pulsar has been extensively observed over a wide frequency range between 100 MHz and 20 GHz. The main pulse is classified as a T type profile with three merged components seen around 1.4 GHz. At lower frequencies the leading conal component is not clearly visible and hence we have used the peak intensities of the central core and the trailing cone to estimate the relative spectral evolution (see Fig. 4, third row, right column). The relative intensity shows a power law spectral dependence between 100 MHz and 8.5 GHz with a comparatively low $\Delta\alpha_{core/cone} \sim -0.2$. At 10 GHz a flattening in the spectra is seen which may be likely due to the merging of the two components as they become indistinguishable at still higher frequencies.

B1946+35 : The pulsar emission is affected by scattering and the profiles show prominent elongated tails below 900 MHz where the individual components cannot be identified. At higher frequencies the presence of a T type profile is seen with a prominent core emission. The leading conal component is merged with the core around 1 GHz but becomes clearly visible at 5 GHz. The peak intensities of the core and trailing core have been used to estimate their relative spectral evolution. Between 900 MHz and 5 GHz the relative intensity show a power law dependence with $\Delta\alpha_{core/cone} \sim -1.5$ (Fig. 4, fourth row, left column).

B2045-16 : The profile is classified as T type with the central core component shifted towards the trailing cone. The emission has been measured over a wide frequency range between 325 MHz and 10 GHz, with the core vanishing at

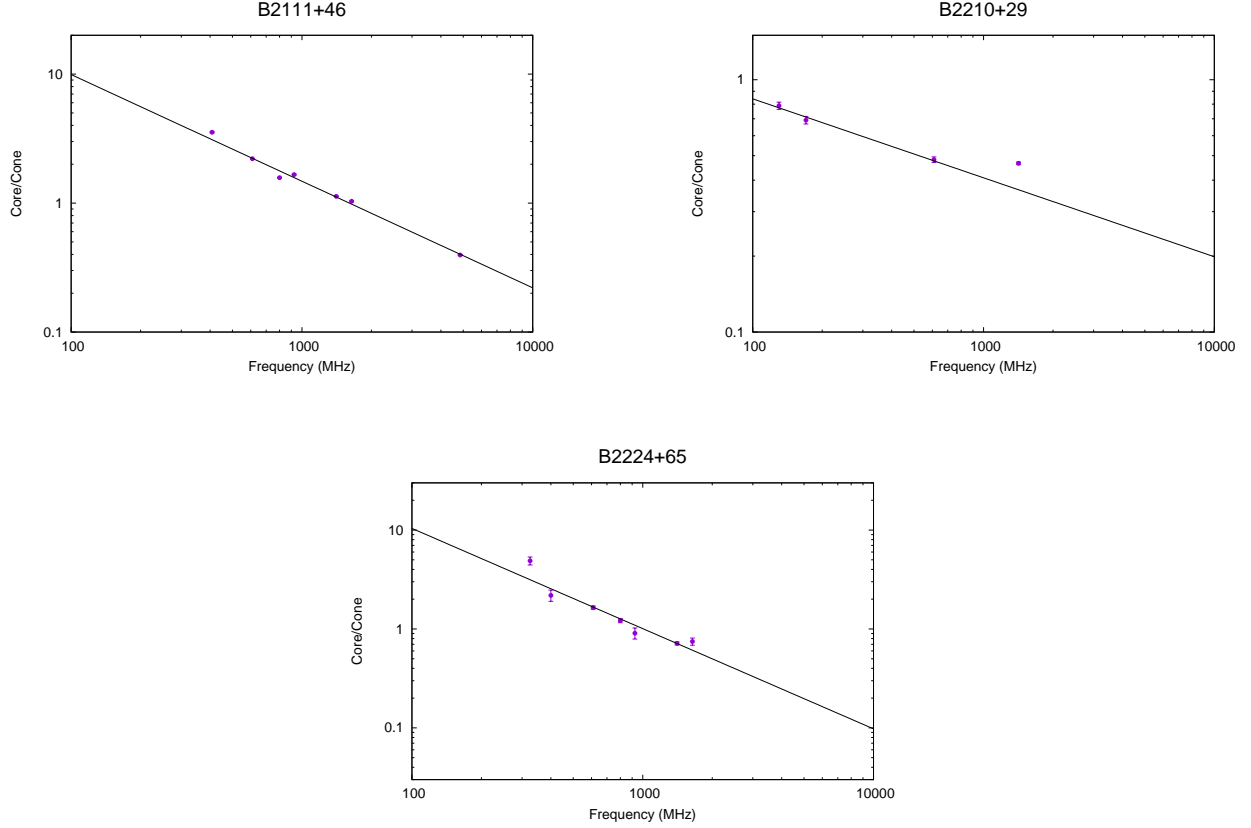


Figure 5. The figure shows the spectral nature of the relative intensities between the core and conal components within the pulsar profile in 3 pulsars between 100 MHz and 10 GHz.

the highest frequencies. The relative intensity between the core and the cones show a power law dependence between 325 MHz and 5 GHz with $\Delta\alpha_{core/cone} \sim -0.5$ (Fig. 4, fourth row, right column).

B2111+46 : The pulsar has a relatively wide profile that occupies more than 20 percent of the period and shows three distinct emission components with T classification (see Fig. 1, right column). The pulsar emission is scattered at frequencies around 100 MHz. The power law dependence is seen for the frequency evolution of the relative intensity between 400 MHz and 5 GHz with $\Delta\alpha_{core/cone} \sim -0.8$ (Fig. 5, upper left panel).

B2210+29 : The pulsar has a T type profile and has many measurements between 100 MHz and 1.6 GHz. However, some of these profiles have lower detection sensitivities where the components cannot be measured. The relative intensity between the core and the cone has a power law dependence between 100 MHz and 600 MHz with $\Delta\alpha_{core/cone} \sim -0.3$ which signifies a relatively flatter behaviour (Fig. 5, upper right panel), and shows further flattening at 1.4 GHz.

B2224+65 : The pulsar has a profile with two emission components and was classified as $T_{1/2}$ with the leading component being the core and the trailing one the cone (Basu et al. 2015). The profiles have been measured over multiple frequencies between 100 MHz and 1.6 GHz, but the cone vanishes around 100 MHz. The detection sensitivities show large variations as a result of which we used the peak intensities for the relative intensity estimates. The relative intensity of the core and the cone shows a power law dependence between 325 MHz and 1.6 GHz with $\Delta\alpha_{core/cone} \sim -1.0$ (see Fig. 5, lower panel).

4. CURVATURE RADIATION

The radio emission in pulsars arises due to coherent curvature radiation from relativistic charge bunches, that are formed due to two stream instability developing in the outflowing plasma (Asseo & Melikidze 1998; Melikidze et al. 2000; Gil et al. 2004). The two stream instability can develop in overlapping clouds of plasma moving along the open magnetic field lines. The presence of an inner acceleration region (IAR), with unscreened electric field, above the polar cap is required to generate a non-stationary flow resulting in the overlapping clouds of plasma. The electron-positron pairs are formed due to magnetic pair creation from high energy photons in the IAR, which gets separated and accelerated into opposite directions by the electric field (Ruderman & Sutherland 1975; Gil et al. 2003). A sparking discharge ensues as a result of additional pair production from curvature radiation and/or inverse Compton scattering of high energy photons from the initial charges (Medin & Lai 2007; Szary et al. 2015). The potential difference along the IAR vanishes over timescales of hundreds of nanoseconds due to the excess charges which inhibits further pair formation. The positrons are accelerated away from the surface to relativistic energies, with Lorentz factors of $\gamma_p \sim 10^6$, forming the primary particles. Once the IAR becomes sufficiently empty due to outflow of the excess charges, the electric field reappears starting the sparking process once again to generate the non-stationary plasma flow.

The primary particles continue to radiate high energy photons as they move along the curved magnetic field lines beyond the IAR, resulting in a pair cascade that forms the secondary plasma comprising of both electron and positron streams. The primary particles outside the IAR has the co-rotation Goldreich-Julian density, n_{GJ} (Goldreich & Julian 1969), while the secondary plasma has Lorentz factors of $\gamma_s \sim 10^2$ and density $n_s = \kappa n_{GJ}$, where $\kappa \geq 10^4$ is the multiplicative factor (Sturrock 1971) and n_{GJ} can be obtained from :

$$\begin{aligned} n_{GJ} &= -(\vec{\Omega} \cdot \vec{B})/2\pi ce \\ &= 5.6 \times 10^5 \left(\frac{\dot{P}_{-15}}{P} \right)^{1/2} R_{50}^{-3} \text{ cm}^{-3} \end{aligned} \quad (2)$$

Here $\vec{\Omega}$ is the angular velocity of stellar rotation, \vec{B} is the magnetic field at a specific location, P is the pulsar period, $\dot{P}_{-15} = \dot{P}/10^{-15}$ with \dot{P} being the rate of period slowdown, $R_{50} = r/50R_S$, where r is the radial distance and $R_S = 10$ km is the radius of the neutron star. The plasma instability develops in the secondary plasma, and its linear and nonlinear growth results in the formation of relativistic charge bunches around heights of 100-1000 km from the surface. As these charge bunches accelerate in the curved magnetic field lines they radiate curvature radiation which is seen as the radio emission.

The curvature of the magnetic field lines at any emission height increases from the magnetic axis towards the edge of the open field line region. The centrally located core component in the emission beam is expected to originate from the field lines close to the magnetic axis, while the inner and outer cones from field lines further away from the axis. In this section we explore the effect of the different magnetic field curvature on the spectra of the curvature radiation. Below we consider two different cases, the first corresponding to spectra of incoherent emission from a distribution of charged particles emitting curvature radiation and the second case deals with curvature radiation from charged solitons. We are primarily concerned with the total spectra obtained from the radiation energy of these sources. However, quantities like the brightness temperature requires estimation of the radiation intensity (see Roy & Gangadhara 2019; Gangadhara et al. 2021). The formation of charged solitons in the pulsar magnetosphere have been worked out in more detail in several works (Melikidze et al. 2000; Lakoba et al. 2018; Yang & Zhang 2018; Rahaman et al. 2020) and is outside the scope of this paper. We use the results from these earlier works to simulate the variation in the spectral nature across the different profile components.

4.1. Incoherent curvature radiation from distribution of charges

We first consider the case of the incoherent curvature radiation from a distribution of charge particles with Lorentz factors equivalent to the secondary plasma, moving along the open dipolar magnetic field lines. This requires suitably adding the radiation energies from all particles visible within the line of sight for all frequencies. The emitted radiation energy (I) at a given frequency (ω) per unit solid angle (Ω) by a relativistically charge particle moving along a curved trajectory can be obtained as (Jackson 1998) :

$$\frac{d^2 I}{d\omega d\Omega} = I_0 \left(\frac{\omega}{\omega_c} \right)^2 (1 + \gamma_s^2 \theta^2)^2 \left[K_{2/3}^2(\xi) + \left(\frac{\gamma_s^2 \theta^2}{1 + \gamma_s^2 \theta^2} \right) K_{1/3}^2(\xi) \right]. \quad (3)$$

where I_0 is the energy at the characteristic frequency (ω_c) emitted along the tangential direction, γ_s is the Lorentz factor of the secondary plasma particle, θ is the angle between the line of sight and the tangential direction of particle

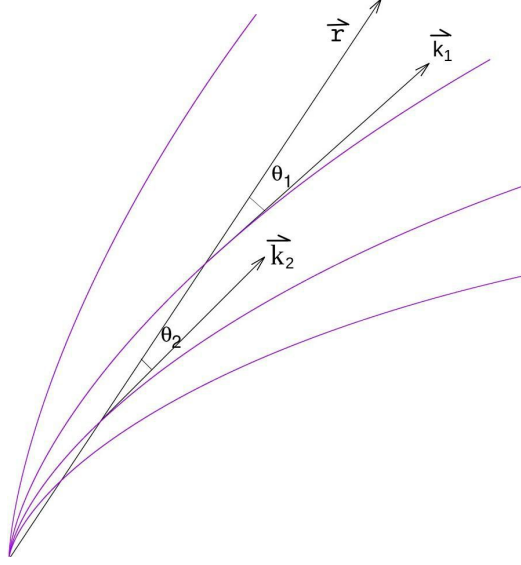


Figure 6. The figure shows a schematic representing the intersection of the line of sight (LOS) along the radial direction (\vec{r}) with the magnetic field lines. The wave vector of the radiation (\vec{k}) is along the tangent to the magnetic field lines and the LOS makes different angles with the the wave vector emitted from different heights, eg. θ_1 and θ_2 as shown here. The curvature radiation around the characteristic frequency is highly beamed and can only be detected over a small angular radius $\theta < 1/\gamma$, where γ is the Lorentz factor of the relativistic particles.

trajectory (see Fig. 6), $K_{1/3}$ and $K_{2/3}$ are modified Bessel functions, and

$$\omega_c = \frac{3}{2}\gamma_s^3 \left(\frac{c}{\rho_c}\right); \quad \xi = \frac{\omega}{2\omega_c} (1 + \gamma_s^2\theta^2)^{3/2} \quad (4)$$

with ρ_c being the radius of curvature of the curved trajectory at the point of emission. The above spectrum peaks around $\omega \sim \omega_c$ and falls off sharply on either side.

In order to estimate the spectra for any particular line of sight, specified by the angle θ , the directed emission from all relevant charges needs to be added for all frequencies. The radio emission is expected to arise between heights of $r = 100$ km and $r = 1000$ km. We consider the angular size of the core, inner cone and outer cone as defined below and average the spectra of all line of sights within each component. These estimates can be compared with the observed spectra as shown in section 3. We have used the following scheme to implement the measurement of spectra in each component.

- A power-law function, $n(\gamma) \propto \gamma^a$, is considered for the relativistic charge particle distribution. For these estimates γ_s is confined between 50 and 300 with index $a = -0.3$.
- The emission is constrained to originate between heights of $10R_S < r < 100R_S$. The radius of curvature at any given point is estimated in Basu et al. (2020a, see appendix).
- At any given height the beam opening angle (θ_b) is obtained as :

$$\sin \theta_b = \left(\frac{r}{R_{LC}}\right)^{1/2} \quad R_{LC} = Pc/2\pi. \quad (5)$$

In order to estimate the spectra across the emission beam we consider the LOS to cut centrally through the magnetic axis across the open field lines (which is indeed the case for M and T type pulsars mostly studied here).

- A relatively simple model of the emission beam is considered with core (ϕ_{cr}), inner cone (ϕ_{in}) and outer cone (ϕ_{out}) at any given height defined as :

$$0 < \phi_{cr} < \theta_b/5, \quad \theta_b/5 < \phi_{in} < 3\theta_b/5, \quad 3\theta_b/5 < \phi_{out} < \theta_b.$$

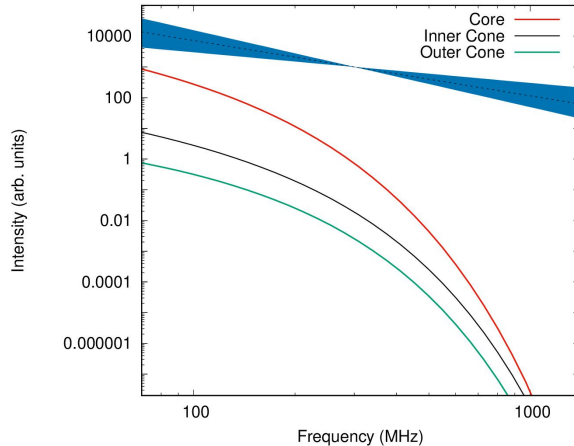


Figure 7. The figure shows the spectra of the different profile components from a distribution of relativistic particles emitting curvature radiation. The shaded region (blue) shows the expected emission spectra in the pulsar population with spectral index usually varying between -1.0 and -2.5 with a median value of -1.8 (dotted line).

In addition the intensities are convolved with Gaussian functions centered around 0 , $2\theta_b/5$ and $4\theta_b/5$ corresponding to the centers of the core, inner and outer cones, respectively, to emulate the observed profiles.

The radiation energies corresponding to all relevant particles within the confines of each component type and over the relevant emission heights are added up to form their respective spectra as shown in Fig. 7. The simulated spectra shows a consistent evolution across the profile with the core component having a steeper spectra compared to the cones. This shows that the variations in the relative spectra between the core and the cones (see section 3) can be naturally explained from curvature radiation over narrow emission heights due to change in the radius of curvature from the axis towards the edge of the open field lines. However, as seen in Fig. 7, the spectra is much steeper than the observed spectra with spectral index being around -4 to -6 between 100 MHz and 1 GHz compared to being around -2.0 in observed cases (Maron et al. 2000). In order to obtain the measured spectra one requires $\gamma \sim 10^3 - 10^4$ that are too high for the secondary plasma in pulsars. It should also be noted that for a distribution of particles incoherent emission from individual particles are possible only when the separation between them is more than the wavelength of the emitted radiation. For longer wavelengths the particles will interact with each other resulting in absorption of radiation. This makes it impossible for the density of plasma in the pulsar magnetosphere to emit incoherent emission, where the average separation between particles $\propto n^{-1/3}$ is much smaller than radio wavelengths. Nonetheless, the purpose of this exercise is to demonstrate the effect of radius of curvature on the spectra of curvature radiation.

4.2. Coherent Curvature radiation from Solitons

The formation of charge separated solitons has been proposed by Melikidze et al. (2000, MGP00 hereafter) as the mechanism for charge bunching in the pulsar magnetosphere. The two stream instability in the outflowing plasma clouds trigger strong Langmuir oscillations in the electron-positron plasma around heights of several hundred kilometers from the stellar surface (Asseo & Melikidze 1998). The amplitude of these waves are modulationally unstable and form packets of high density regions in the form of solitons. In the charge separated pulsar magnetosphere a natural difference arises between the energy distribution of electrons and positrons resulting in non-zero $\Delta\gamma = |\gamma_- - \gamma_+|$, such that the relativistic mass difference between the two species produces inertial charge separation within the soliton envelope. These charge separated solitons emit coherent curvature radiation as they move along the open magnetic field lines. We use the details of soliton characteristics as described in MGP00 to simulate the spectra in the different profile components.

The typical longitudinal length scales of solitons along the magnetic field lines can be estimated as (see eq. 10 in MGP00) :

$$\Delta_s \sim 40\gamma_2^{0.5}\kappa_4^{-0.5}R_{50}^{1.5}\Delta_d\chi^{-0.5}P^{0.25}\dot{P}_{-15}^{-0.25} \text{ cm}, \quad (6)$$

where $\gamma_2 = \gamma_s/100$, $\kappa_4 = \kappa/10^4$, $\Delta_d \sim 0.5$ is a dimensionless parameter and $\chi \sim 0.1$ is related to the growth rate of the waves in the plasma. The typical length scales of solitons are around 10 to 100 cm which ensures the emission of coherent radio emission ($\lambda > \Delta_s$). The spectrum of the total energy emitted by solitons can be estimated as :

$$\frac{d^2 I}{d\omega d\Omega} = \frac{Q^2}{c} \omega_o F\left(\frac{\omega}{\omega_o}, \theta\right) \left[1 - \cos\left(a \frac{\omega}{\omega_o}\right)\right]^2 \quad (7)$$

Here Q is the total charge in solitons, $\omega_o = \frac{3}{2} \gamma_o^3 / \rho_c$, $a = \gamma_o^3 (\Delta_s / \rho_c)$ and

$$F\left(\frac{\omega}{\omega_o}, \theta\right) = \left(\frac{\omega}{\omega_o}\right)^2 (1 + \gamma_o^2 \theta^2)^2 \left[K_{2/3}^2(\xi) + \left(\frac{\gamma_o^2 \theta^2}{1 + \gamma_o^2 \theta^2}\right) K_{1/3}^2(\xi) \right], \quad \xi = \frac{\omega}{2\omega_o} (1 + \gamma_o^2 \theta^2)^{3/2}. \quad (8)$$

In comparison with the single particle curvature radiation the soliton spectra has an extra term $[1 - \cos(a(\omega/\omega_o))]^2$ which shifts the peak frequency by a factor of ~ 4 from ω_o and makes the curve wider and more symmetrical (see Fig. 4 in MGP00). In addition the Lorentz factors of solitons γ_o corresponds to the group velocities of the wave packets and are usually greater than the Lorentz factors of the secondary plasma particles, $\gamma_o = y\gamma_s$, with $y \sim 2$. As a result the characteristic frequencies of solitons ω_o are almost an order of magnitude greater than the single particle ω_c . This further highlights the applicability of the soliton model as a viable mechanism for pulsar emission since the peak frequencies of soliton spectra are around 100-1000 MHz which are between one and two orders of magnitude higher than the single particle case. Using basic pulsar parameters MGP00 estimated the spectra of the coherent curvature radiation energy from each soliton as :

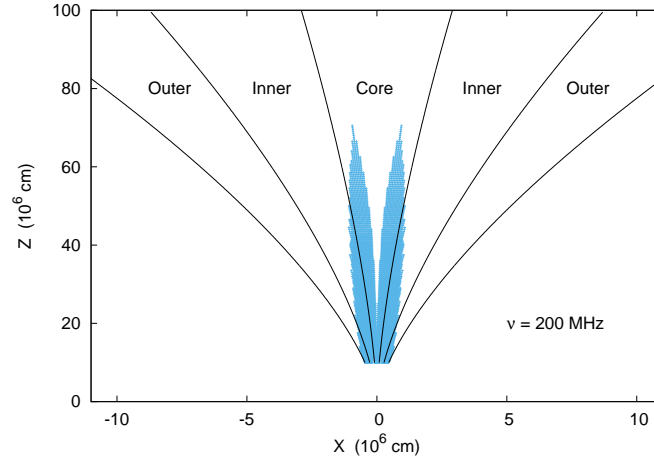
$$\frac{d^2 I}{d\omega d\Omega} = A_1 \gamma_2 \kappa_4 R_{50}^{2.5} \chi^3 P^{-3/7} \dot{P}_{-15}^{-9/14} F\left(\frac{\omega}{\omega_o}, \theta\right) \left[1 - \cos\left(a \frac{\omega}{\omega_o}\right)\right]^2 \text{ ergs Hz}^{-1} \text{ sr}^{-1}, \quad (9)$$

and the total number of solitons contributing to the pulsar emission at any instant to be :

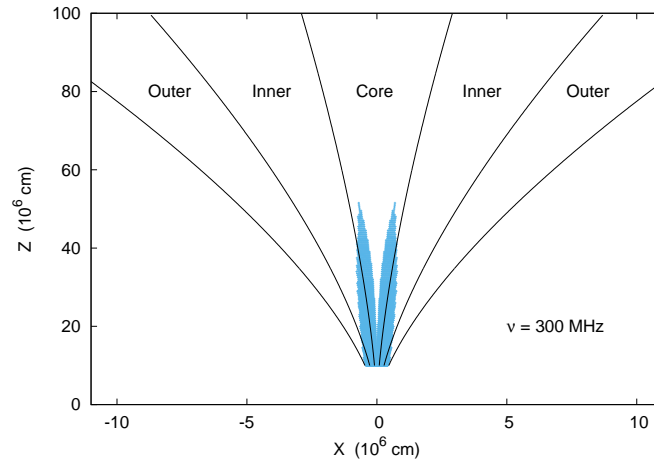
$$N_s \sim 10^5 \gamma_2^{-0.5} \kappa_4 R_{50}^{-0.5} \Delta_d^{-1} \chi^{0.5} P^{-1/4} \dot{P}_{-15}^{-1/4}. \quad (10)$$

The total energy of coherent curvature radiation emitted at any frequency can be obtained from $N_s dI/d\omega$. We are primarily interested in the relative difference of the spectra and the absolute values of the energy is contained in the constant term A_1 . The soliton spectra obtained from eq.(9) and (10) is dependent on a number of parameters that are likely to have a range of values, e.g. the variability of soliton lengths, the Lorentz factors of solitons, the distribution of secondary pair plasma, the optimal emission heights for the plasma instabilities to develop and their frequency dependence, the growth factor of the plasma waves, soliton charge densities, etc. It is unlikely that the full extent of how these parameters vary can be estimated from observational constraints alone and would require more detailed modelling of the non-linear plasma instabilities (see for e.g. [Lakoba et al. 2018](#); [Rahaman et al. 2020](#)) which is outside the scope of this paper. It is expected that most of these parameters will vary as a function of distance as well as across different field lines. However, our objective in this exercise is to determine if it is possible to obtain the observed variation in spectra seen across different components within the pulsar emission beam by using coherent curvature radiation from solitons. A similar process as explained for the incoherent case was followed to estimate the total radiation energy spectra across each component type, the core, the inner cone and the outer cone. We describe below the steps of estimating the spectra for different components using the above setup.

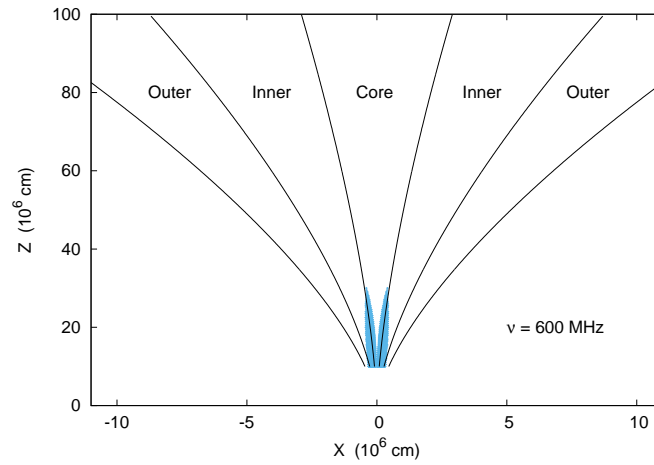
- The emission is once gain constrained to originate between heights of $10R_S < r < 100R_S$.
- The emission beam model is identical to the one used for the single particle curvature radiation described earlier, comprising of a central core between $0 < \phi_{cr} < \theta_b/5$, an inner cone between $\theta_b/5 < \phi_{in} < 3\theta_b/5$ and an outer cone with $3\theta_b/5 < \phi_{out} < \theta_b$, where θ_b is defined in eq.(5). We consider a central LOS traverse across the beam and approximate the components to have Gaussian shapes.
- For most parameters we use a fixed set of values as prescribed in MGP00. The only variable parameter is the Lorentz factors of secondary plasma γ which are allowed to have different set of values around $\gamma \sim 100$ in order to vary the shape of spectra across the components. We once again consider a power law distribution for the Lorentz factors with index $a = -0.3$. The range of γ used for the core is between 50 and 170, the inner cone between 50 and 280, and the outer cone with variations from 5 to 130.



(a)



(b)



(c)

Figure 8. The figure represents the projection of the open field line region for an aligned rotator along the x - z plane where the shaded (blue) area corresponds to the location of the simulated coherent curvature radio emission at (a) 200 MHz, (b) 300 MHz and (c) 600 MHz. The lower limit for the emission height is fixed at 100 km (10^7 cm) and the boundaries of the regions corresponding to the core, inner cone and outer cone used in estimating the spectra are also shown.

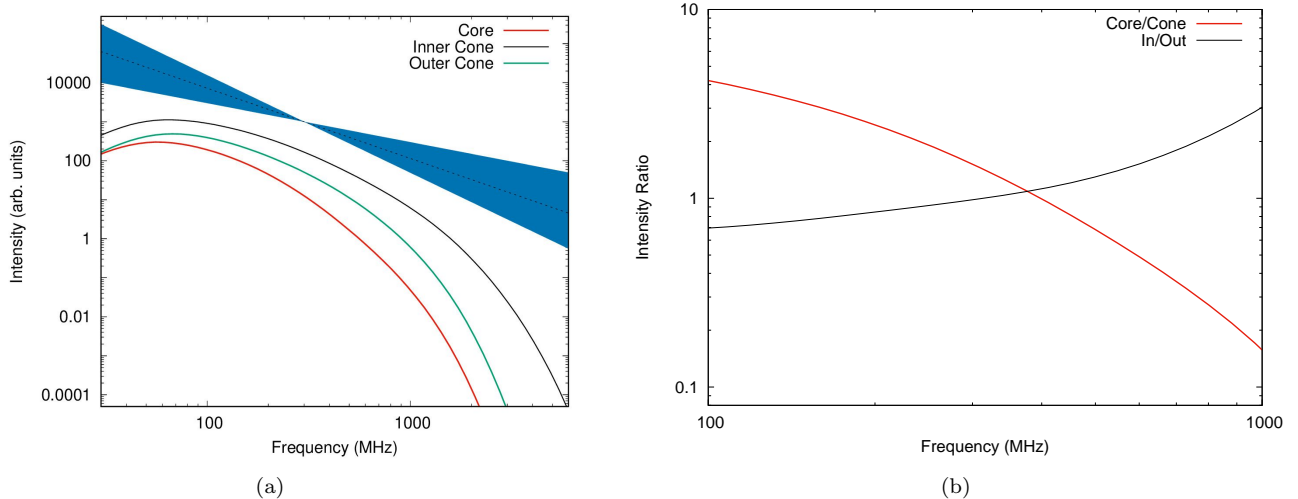


Figure 9. The figure shows the variation in the spectra across the pulse window due to coherent curvature radiation from charged solitons. (a) The spectra of the core, inner cone and outer conal components. The shaded region (blue) shows the expected spectral nature of emission in the pulsar population with spectral index usually varying between -1.0 and -2.5 with a median value of -1.8 (dotted line). (b) the frequency evolution of the relative intensities in the core and cone as well as the inner and outer cones. The ratios of the intensities have been scaled to fit within the window.

We are primarily interested in the behaviour of the spectra within the frequency range 100 MHz and 1 GHz where the relative component spectra are well constrained. The region from where a particular frequency is emitted depends on ω_o which is a function of the radius of curvature and γ_o . The radius of curvature further depends on the emission height as well as the distance from the magnetic axis. For any given γ_o the emission along any field line is directed towards the observer when the angle between the radial vector (\vec{r}) and the tangent to the field line at the point of emission is less than $1/\gamma_o$ (see Fig. 6). This introduces an additional constraint on the emission between the inner magnetic field lines, closer to the magnetic axis and the outer field lines further away particularly those for the outer cones where the curvature is higher resulting in larger angles. Fig. 8 shows the area of the open field line region where the radio emission arises from at different frequencies of 200 MHz, 300 MHz and 600 MHz for our selected setup of emission parameters. We divided the open field line region between emission heights of 100 to 1000 km into small grids and separately estimated the spectra in each grid. For any given frequency if significant emission was seen at a grid, i.e. more than 1 percent of power of the grid with maximum energy for that frequency, it was marked with a blue point and shown in the figure. At the lower frequencies the emission can originate from much higher r , while the emission is restricted to much lower r in the outer cones across all frequencies. Fig. 9 shows the estimated spectra for the core, inner cone and outer cones. The core emission is steeper than the cones due to variation in the curvature which is also seen for the single particle case. The outer cones also have steeper spectra than the inner cones as a result of the beaming effect such that emission from certain field lines at higher frequencies are not directed towards the observer making the spectra steeper. The spectral index for the inner cone between 100 MHz and 1 GHz is -2.0 (9, left panel), which is consistent with observations. In addition $\Delta\alpha_{core/cone} \sim -1.2$ and $\Delta\alpha_{in/out} \sim +0.6$ (9, right panel) which matches the observational results in section 3. It should be noted that the physical parameters used in these simulations of spectra are demonstrative in nature and do not represent unique solutions regarding the physical conditions in the pulsar magnetosphere.

5. CONCLUSION

The relative spectral index between the core and the conal emission has been estimated by Basu et al. (2021) in 21 pulsars over a relatively narrow frequency range between 325 MHz and 610 MHz. They found the core emission to be relatively steeper than the cones with mean relative spectral index of $\Delta\alpha_{core/cone} \sim -0.7$. The outer cone also showed a steeper spectra than the inner cone such that $\Delta\alpha_{in/out} \sim +0.4$. In this work we have used average profile measurements from archival observations to expand the above studies in a larger sample of 53 pulsars with much wider frequency coverage between 100 MHz and 10 GHz. In all cases we found the core component to have a steeper spectra compared to the core, although the differences in spectra show a relatively uniform distribution between -0.2 and

–2.0. In 9 pulsars we were able to measure the the spectral difference between the inner and the outer cones, with the inner cone being less steep than the outer cone with relative spectral index between +0.1 and +0.8. In a few cases the differences in spectra show flattening at higher frequencies above 1 GHz. However, in almost all such cases we found that these were a result of some of the components merging together at higher frequencies thereby affecting relative intensity estimates. Our analysis clearly highlight the evolution of the pulsar spectra within the emission window in the entire pulsar population as no clear correlation is seen between the relative spectral index and different pulsar parameters.

The radio emission in pulsars is expected to originate within a narrow range of heights, a few hundred kilometers from the stellar surface, due to coherent curvature radiation. This requires the formation of charged bunches in the form of charge separated solitons due to non-linear instabilities in the outflowing plasma. A natural steepening of the spectra is expected due to increase of curvature of the magnetic field lines from the axis towards the edge of the open field lines. Further, the relativistic beaming effect restricts the emission at the outermost field lines from being directed towards the observer. This mostly affects the higher frequencies which are supposed to be emitted by particles with higher Lorentz factors. As a result additional steepening of the spectra is expected for the outermost field lines compared to relatively inner ones. The above mechanism can explain the variations in spectra seen in the pulsar emission window if one considers the core to arise from field lines close to the magnetic axis, the inner cones from field lines further away from the core, while the outer cones are furthest away and located near the edge of the open field line region.

The plasma populating the open field line region originates due to sparking discharges in an inner acceleration region (IAR) above the polar cap. The sparking process is thermally regulated due to discharge of ions from the heated polar cap surface forming a partially screened gap (PSG, Gil et al. 2003; Szary et al. 2015). Differences in the expected potential drop along the IAR can arise from the center of the IAR towards the polar cap edge due to the distribution of sparks. The center is populated by sparks from all sides and is likely to have a larger potential drop, while the thermal regulation requires the presence of a spark always near the rim of the polar cap which likely has reduced potential difference along the gap (Gil & Sendyk 2000; Basu et al. 2020a). As a result the distribution function of the outflowing plasma generated from the sparks can show variations between the central regions and the outer field lines. Our studies show that such variations are likely to affect the relative differences in spectra across the profile. However, the emission mechanism is dependent on a number of parameters which are not well constrained. More detailed modelling of the nonlinear plasma processes are required to narrow the range of these parameters before such association between the variations in spectra and the plasma distribution function can be studied in more detail.

ACKNOWLEDGMENTS

We thank the referee for comments that helped to improve the paper. DM acknowledges the support of the Department of Atomic Energy, Government of India, under project no. 12-R&D-TFR-5.02-0700. DM acknowledges funding from the grant “Indo-French Centre for the Promotion of Advanced Research - CEFIPRA” grant IFC/F5904-B/2018. This work was supported by the grant 2020/37/B/ST9/02215 of the National Science Centre, Poland.

REFERENCES

- Arzoumanian, Z., Nice, D. J., Taylor, J. H., & Thorsett, S. E. 1994, *ApJ*, 422, 671, doi: [10.1086/173760](https://doi.org/10.1086/173760)
- Asseo, E., & Melikidze, G. I. 1998, *MNRAS*, 301, 59, doi: [10.1046/j.1365-8711.1998.01990.x](https://doi.org/10.1046/j.1365-8711.1998.01990.x)
- Basu, R., & Mitra, D. 2018, *MNRAS*, 475, 5098, doi: [10.1093/mnras/sty178](https://doi.org/10.1093/mnras/sty178)
- Basu, R., Mitra, D., & Melikidze, G. I. 2020a, *MNRAS*, 496, 465, doi: [10.1093/mnras/staa1574](https://doi.org/10.1093/mnras/staa1574)
- . 2020b, *ApJ*, 889, 133, doi: [10.3847/1538-4357/ab63c9](https://doi.org/10.3847/1538-4357/ab63c9)
- . 2021, *ApJ*, 917, 48, doi: [10.3847/1538-4357/ac0828](https://doi.org/10.3847/1538-4357/ac0828)
- Basu, R., Mitra, D., Melikidze, G. I., & Skrzypczak, A. 2019, *MNRAS*, 482, 3757, doi: [10.1093/mnras/sty2846](https://doi.org/10.1093/mnras/sty2846)
- Basu, R., Mitra, D., & Rankin, J. M. 2015, *ApJ*, 798, 105, doi: [10.1088/0004-637X/798/2/105](https://doi.org/10.1088/0004-637X/798/2/105)
- Bilous, A. V., Kondratiev, V. I., Kramer, M., et al. 2016, *A&A*, 591, A134, doi: [10.1051/0004-6361/201527702](https://doi.org/10.1051/0004-6361/201527702)
- Blaskiewicz, M., Cordes, J. M., & Wasserman, I. 1991, *ApJ*, 370, 643, doi: [10.1086/169850](https://doi.org/10.1086/169850)
- D’Amico, N., Stappers, B. W., Bailes, M., et al. 1998, *MNRAS*, 297, 28, doi: [10.1046/j.1365-8711.1998.01397.x](https://doi.org/10.1046/j.1365-8711.1998.01397.x)
- Gangadhara, R. T., Han, J. L., & Wang, P. F. 2021, *ApJ*, 911, 152, doi: [10.3847/1538-4357/abe714](https://doi.org/10.3847/1538-4357/abe714)
- Gil, J., Lyubarsky, Y., & Melikidze, G. I. 2004, *ApJ*, 600, 872, doi: [10.1086/379972](https://doi.org/10.1086/379972)

- Gil, J., Melikidze, G. I., & Geppert, U. 2003, *A&A*, 407, 315, doi: [10.1051/0004-6361:20030854](https://doi.org/10.1051/0004-6361:20030854)
- Gil, J. A., & Sendyk, M. 2000, *ApJ*, 541, 351, doi: [10.1086/309394](https://doi.org/10.1086/309394)
- Goldreich, P., & Julian, W. H. 1969, *ApJ*, 157, 869, doi: [10.1086/150119](https://doi.org/10.1086/150119)
- Gould, D. M., & Lyne, A. G. 1998, *MNRAS*, 301, 235, doi: [10.1046/j.1365-8711.1998.02018.x](https://doi.org/10.1046/j.1365-8711.1998.02018.x)
- Jackson, J. D. 1998, *Classical Electrodynamics*, 3rd Edition
- Jankowski, F., van Straten, W., Keane, E. F., et al. 2018, *MNRAS*, 473, 4436, doi: [10.1093/mnras/stx2476](https://doi.org/10.1093/mnras/stx2476)
- Johnston, S., Karastergiou, A., & Willett, K. 2006, *MNRAS*, 369, 1916, doi: [10.1111/j.1365-2966.2006.10440.x](https://doi.org/10.1111/j.1365-2966.2006.10440.x)
- Johnston, S., & Kerr, M. 2018, *MNRAS*, 474, 4629, doi: [10.1093/mnras/stx3095](https://doi.org/10.1093/mnras/stx3095)
- Karastergiou, A., & Johnston, S. 2006, *MNRAS*, 365, 353, doi: [10.1111/j.1365-2966.2005.09692.x](https://doi.org/10.1111/j.1365-2966.2005.09692.x)
- Kijak, J., & Gil, J. 1998, *MNRAS*, 299, 855, doi: [10.1046/j.1365-8711.1998.01832.x](https://doi.org/10.1046/j.1365-8711.1998.01832.x)
- . 2003, *A&A*, 397, 969, doi: [10.1051/0004-6361:20021583](https://doi.org/10.1051/0004-6361:20021583)
- Kijak, J., Kramer, M., Wielebinski, R., & Jessner, A. 1998, *A&AS*, 127, 153, doi: [10.1051/aas:1998340](https://doi.org/10.1051/aas:1998340)
- Kou, F. F., Yan, W. M., Peng, B., et al. 2021, *ApJ*, 909, 170, doi: [10.3847/1538-4357/abd545](https://doi.org/10.3847/1538-4357/abd545)
- Kramer, M., Xilouris, K. M., Jessner, A., et al. 1997, *A&A*, 322, 846
- Krzyszowski, K., Mitra, D., Gupta, Y., et al. 2009, *MNRAS*, 393, 1617, doi: [10.1111/j.1365-2966.2008.14287.x](https://doi.org/10.1111/j.1365-2966.2008.14287.x)
- Lakoba, T., Mitra, D., & Melikidze, G. 2018, *MNRAS*, 480, 4526, doi: [10.1093/mnras/sty2152](https://doi.org/10.1093/mnras/sty2152)
- Lorimer, D. R., Yates, J. A., Lyne, A. G., & Gould, D. M. 1995, *MNRAS*, 273, 411, doi: [10.1093/mnras/273.2.411](https://doi.org/10.1093/mnras/273.2.411)
- Maciesiak, K., Gil, J., & Melikidze, G. 2012, *MNRAS*, 424, 1762, doi: [10.1111/j.1365-2966.2012.21246.x](https://doi.org/10.1111/j.1365-2966.2012.21246.x)
- Maron, O., Kijak, J., Kramer, M., & Wielebinski, R. 2000, *A&AS*, 147, 195, doi: [10.1051/aas:2000298](https://doi.org/10.1051/aas:2000298)
- Medin, Z., & Lai, D. 2007, *MNRAS*, 382, 1833, doi: [10.1111/j.1365-2966.2007.12492.x](https://doi.org/10.1111/j.1365-2966.2007.12492.x)
- Melikidze, G. I., Gil, J. A., & Pataraya, A. D. 2000, *ApJ*, 544, 1081, doi: [10.1086/317220](https://doi.org/10.1086/317220)
- Melikidze, G. I., Mitra, D., & Gil, J. 2014, *ApJ*, 794, 105, doi: [10.1088/0004-637X/794/2/105](https://doi.org/10.1088/0004-637X/794/2/105)
- Mitra, D. 2017, *Journal of Astrophysics and Astronomy*, 38, 52, doi: [10.1007/s12036-017-9457-6](https://doi.org/10.1007/s12036-017-9457-6)
- Mitra, D., Basu, R., Maciesiak, K., et al. 2016, *ApJ*, 833, 28, doi: [10.3847/1538-4357/833/1/28](https://doi.org/10.3847/1538-4357/833/1/28)
- Mitra, D., & Deshpande, A. A. 1999, *A&A*, 346, 906, <https://arxiv.org/abs/astro-ph/9904336>
- Mitra, D., Gil, J., & Melikidze, G. I. 2009, *ApJL*, 696, L141, doi: [10.1088/0004-637X/696/2/L141](https://doi.org/10.1088/0004-637X/696/2/L141)
- Mitra, D., & Li, X. H. 2004, *A&A*, 421, 215, doi: [10.1051/0004-6361:20034094](https://doi.org/10.1051/0004-6361:20034094)
- Mitra, D., & Rankin, J. M. 2002, *ApJ*, 577, 322, doi: [10.1086/342136](https://doi.org/10.1086/342136)
- . 2011, *ApJ*, 727, 92, doi: [10.1088/0004-637X/727/2/92](https://doi.org/10.1088/0004-637X/727/2/92)
- Olszanski, T. E. E., Mitra, D., & Rankin, J. M. 2019, *MNRAS*, 489, 1543, doi: [10.1093/mnras/stz2172](https://doi.org/10.1093/mnras/stz2172)
- Phillips, J. A. 1992, *ApJ*, 385, 282, doi: [10.1086/170936](https://doi.org/10.1086/170936)
- Pilia, M., Hessels, J. W. T., Stappers, B. W., et al. 2016, *A&A*, 586, A92, doi: [10.1051/0004-6361/201425196](https://doi.org/10.1051/0004-6361/201425196)
- Radhakrishnan, V., & Cooke, D. J. 1969, *Astrophys. Lett.*, 3, 225
- Rahaman, S. M., Mitra, D., & Melikidze, G. I. 2020, *MNRAS*, 497, 3953, doi: [10.1093/mnras/staa2280](https://doi.org/10.1093/mnras/staa2280)
- Rankin, J. M. 1983, *ApJ*, 274, 333, doi: [10.1086/161450](https://doi.org/10.1086/161450)
- . 1990, *ApJ*, 352, 247, doi: [10.1086/168530](https://doi.org/10.1086/168530)
- . 1993, *ApJ*, 405, 285, doi: [10.1086/172361](https://doi.org/10.1086/172361)
- Rankin, J. M., & Rathnasree, N. 1997, *Journal of Astrophysics and Astronomy*, 18, 91, doi: [10.1007/BF02714873](https://doi.org/10.1007/BF02714873)
- Rickett, B. J. 1990, *ARA&A*, 28, 561, doi: [10.1146/annurev.aa.28.090190.003021](https://doi.org/10.1146/annurev.aa.28.090190.003021)
- Roy, T., & Gangadhara, R. T. 2019, *ApJ*, 878, 148, doi: [10.3847/1538-4357/ab1fe5](https://doi.org/10.3847/1538-4357/ab1fe5)
- Ruderman, M. A., & Sutherland, P. G. 1975, *ApJ*, 196, 51, doi: [10.1086/153393](https://doi.org/10.1086/153393)
- Seiradakis, J. H., Gil, J. A., Graham, D. A., et al. 1995, *A&AS*, 111, 205
- Skrzypczak, A., Basu, R., Mitra, D., et al. 2018, *ApJ*, 854, 162, doi: [10.3847/1538-4357/aaa758](https://doi.org/10.3847/1538-4357/aaa758)
- Stairs, I. H., Thorsett, S. E., & Camilo, F. 1999, *ApJS*, 123, 627, doi: [10.1086/313245](https://doi.org/10.1086/313245)
- Sturrock, P. A. 1971, *ApJ*, 164, 529, doi: [10.1086/150865](https://doi.org/10.1086/150865)
- Szary, A., Melikidze, G. I., & Gil, J. 2015, *MNRAS*, 447, 2295, doi: [10.1093/mnras/stu2622](https://doi.org/10.1093/mnras/stu2622)
- von Hoensbroech, A., & Xilouris, K. M. 1997, *A&AS*, 126, 121
- Weisberg, J. M., Cordes, J. M., Lundgren, S. C., et al. 1999, *ApJS*, 121, 171, doi: [10.1086/313189](https://doi.org/10.1086/313189)
- Weltevrede, P., & Johnston, S. 2008, *MNRAS*, 391, 1210, doi: [10.1111/j.1365-2966.2008.13950.x](https://doi.org/10.1111/j.1365-2966.2008.13950.x)
- Wu, X., Manchester, R. N., Lyne, A. G., & Qiao, G. 1993, *MNRAS*, 261, 630, doi: [10.1093/mnras/261.3.630](https://doi.org/10.1093/mnras/261.3.630)
- Xilouris, K. M., Kramer, M., Jessner, A., Wielebinski, R., & Timofeev, M. 1996, *A&A*, 309, 481
- Yang, Y.-P., & Zhang, B. 2018, *ApJ*, 868, 31, doi: [10.3847/1538-4357/aae685](https://doi.org/10.3847/1538-4357/aae685)

Table 3. Component Spectral difference

PSR	Type	Freq (MHz)	S_{core}/S_{cone}	$\Delta\alpha$	S_{core}/S_{in}	$\Delta\alpha$	S_{core}/S_{out}	$\Delta\alpha$	S_{in}/S_{out}	$\Delta\alpha$	Ref.
1 B0203-40	$T_{1/2}$	325	11.9 ± 0.9	-0.53 ± 0.07	—	—	—	—	—	—	[1]
		1400	5.5 ± 0.4	—	—	—	—	—	—	—	[2]
2 B0329+54	T	140	4.076 ± 0.007	-0.72 ± 0.06	—	—	—	—	—	—	[3]
		408	6.830 ± 0.006	(408-2250)	—	—	—	—	—	—	[4]
		610	5.555 ± 0.002	—	—	—	—	—	—	—	[4]
		925	3.926 ± 0.004	—	—	—	—	—	—	—	[4]
		1410	2.339 ± 0.002	—	—	—	—	—	—	—	[5]
		1642	2.707 ± 0.005	—	—	—	—	—	—	—	[4]
		2250	2.190 ± 0.004	—	—	—	—	—	—	—	[6]
4850	—	4850	3.265 ± 0.004	—	—	—	—	—	—	—	[5]
		8500	3.5 ± 0.1	—	—	—	—	—	—	—	[6]
		10550	1.72 ± 0.02	—	—	—	—	—	—	—	[8]
3 B0450+55	T	325	3.27 ± 0.01	-0.41 ± 0.02	—	—	—	—	—	—	[7]
		408	2.91 ± 0.06	(325-1642)	—	—	—	—	—	—	[4]
		610	2.39 ± 0.02	—	—	—	—	—	—	—	[4]
		910	2.08 ± 0.03	—	—	—	—	—	—	—	[4]
		1400	1.809 ± 0.006	—	—	—	—	—	—	—	[8]
		1642	1.71 ± 0.05	—	—	—	—	—	—	—	[4]
4850	—	4850	1.41 ± 0.02	—	—	—	—	—	—	—	[5]
		410	0.9 ± 0.1	-0.72 ± 0.06	—	—	—	—	—	—	[4]
		610	0.60 ± 0.03	—	—	—	—	—	—	—	[4]
1408	—	1408	0.33 ± 0.01	—	—	—	—	—	—	—	[4]
		170	4.2 ± 0.1	-1.03 ± 0.05	—	—	—	—	—	—	[9]
		325	4.79 ± 0.09	(325-610)	—	—	—	—	—	—	[1]
610	—	610	2.51 ± 0.06	—	—	—	—	—	—	—	[1]
		4850	0.99 ± 0.03	—	—	—	—	—	—	—	[10]
6 B0844-35	cQ	325	—	—	—	—	—	1.60 ± 0.02	0.61 ± 0.03	—	[1]

Table 3 continued on next page

Table 3 (continued)

PSR	Type	Freq (MHz)	S_{core}/S_{cone}	$\Delta\alpha$	S_{core}/S_{in}	$\Delta\alpha$	S_{core}/S_{out}	$\Delta\alpha$	S_{in}/S_{out}	$\Delta\alpha$	Ref.
		610	—	—	—	—	—	—	2.34±0.04	—	[1]
7	B0919+06	T	4.84±0.03	-0.60±0.01	—	—	—	—	—	—	[3]
		325	2.90±0.01	—	—	—	—	—	—	—	[1]
		610	1.94±0.01	—	—	—	—	—	—	—	[1]
8	B0940-55	T	3.60±0.02	-1.40±0.04	—	—	—	—	—	—	[2]
		3100	1.19±0.04	—	—	—	—	—	—	—	[11]
9	J1034-3224	cQ	—	—	—	—	—	—	0.617±0.003	0.78±0.05	[1]
		408	—	—	—	—	—	—	0.766±0.008	(325-610)	[12]
		610	—	—	—	—	—	—	1.024±0.005	—	[1]
		1400	—	—	—	—	—	—	0.798±0.007	—	[2]
10	B1046-58	cT	—	—	—	—	—	—	1.545±0.004	0.22±0.02	[2]
		8356	—	—	—	—	—	—	2.28±0.03	—	[13]
11	J1141-3322	T	9.9±1.0	-1.61±0.14	—	—	—	—	—	—	[14]
		1400	1.51±0.06	—	—	—	—	—	—	—	[2]
12	B1154-62	T	5.29±0.03	-1.50±0.06	—	—	—	—	—	—	[2]
		3100	1.61±0.07	—	—	—	—	—	—	—	[11]
13	B1237+25	M	1.044±0.003	-0.32±0.04	1.413±0.006	-0.46±0.06	0.950±0.003	-0.29±0.04	0.673±0.002	0.15±0.03	[9]
		180	0.966±0.007	(120-610)	1.23±0.01	(120-610)	0.880±0.006	(120-610)	0.715±0.006	(120-610)	[9]
		325	0.727±0.002	—	0.822±0.002	—	0.680±0.001	—	0.827±0.001	—	[1]
		610	0.648±0.004	—	0.716±0.005	—	0.612±0.004	—	0.855±0.003	—	[1]
		1400	0.709±0.002	—	0.637±0.002	—	0.758±0.002	—	1.190±0.002	—	[8]
14	B1323-58	T _{1/2}	6.20±0.08	-1.64±0.08	—	—	—	—	—	—	[11]
		3100	1.63±0.04	—	—	—	—	—	—	—	[11]
		8356	0.43±0.08	—	—	—	—	—	—	—	[13]
15	B1325-49	M	0.102±0.001	-0.28±0.04	0.367±0.005	-0.36±0.04	0.142±0.001	-0.24±0.04	0.387±0.003	0.12±0.02	[1]

Table 3 continued on next page

Table 3 (continued)

PSR	Type	Freq (MHz)	$S_{\text{core}}/S_{\text{cone}}$	$\Delta\alpha$	$S_{\text{core}}/S_{\text{in}}$	$\Delta\alpha$	$S_{\text{core}}/S_{\text{out}}$	$\Delta\alpha$	$S_{\text{in}}/S_{\text{out}}$	$\Delta\alpha$	Ref.
		610	0.086 ± 0.002		0.292 ± 0.007		0.122 ± 0.002		0.417 ± 0.005		[1]
16	B1353-62	T	1.012 ± 0.003	-1.86 ± 0.02	—	—	—	—	—	—	[2]
		3100	0.231 ± 0.005		—	—	—	—	—	—	[11]
17	B1508+55	T	8.791 ± 0.004	-0.78 ± 0.08	—	—	—	—	—	—	[9]
		180	6.895 ± 0.003		—	—	—	—	—	—	[9]
		325	4.591 ± 0.003		—	—	—	—	—	—	[15]
18	B1541+09	T	26.5 ± 0.5	-1.22 ± 0.06	—	—	—	—	—	—	[9]
		180	18.8 ± 0.6		—	—	—	—	—	—	[9]
		610	4.66 ± 0.06		—	—	—	—	—	—	[4]
		800	2.89 ± 0.06		—	—	—	—	—	—	[16]
		1418	2.139 ± 0.008		—	—	—	—	—	—	[17]
19	J1557-4258	T	7.4 ± 0.3	-0.72 ± 0.05	—	—	—	—	—	—	[1]
		1400	4.11 ± 0.06		—	—	—	—	—	—	[2]
20	B1556-44	T	11.8 ± 0.8	-0.64 ± 0.13	—	—	—	—	—	—	[1]
		1400	5.42 ± 0.03		—	—	—	—	—	—	[2]
		1560	3.6 ± 0.1		—	—	—	—	—	—	[18]
21	B1600-49	T	9.0 ± 0.2	-0.34 ± 0.04	—	—	—	—	—	—	[1]
		1400	6.81 ± 0.06		—	—	—	—	—	—	[2]
22	J1625-4048	T	0.88 ± 0.01	-0.83 ± 0.23	—	—	—	—	—	—	[12]
		610	0.576 ± 0.002		—	—	—	—	—	—	[1]
		1400	0.36 ± 0.02		—	—	—	—	—	—	[12]
23	B1642-03	T	52.1 ± 0.4	-1.39 ± 0.05	—	—	—	—	—	—	[1]
		1400	14.7 ± 0.3		—	—	—	—	—	—	[2]
		4850	3.07 ± 0.07		—	—	—	—	—	—	[5]
		10550	1.05 ± 0.07		—	—	—	—	—	—	[8]

Table 3 continued on next page

Table 3 (continued)

PSR	Type	Freq (MHz)	S_{score}/S_{score}	$\Delta\alpha$	S_{score}/S_{in}	$\Delta\alpha$	S_{score}/S_{out}	$\Delta\alpha$	S_{in}/S_{out}	$\Delta\alpha$	Ref.
24	B1700-32	325	0.601 ± 0.001	-0.477 ± 0.005	—	—	—	—	—	—	[1]
		610	0.445 ± 0.001	—	—	—	—	—	—	—	[1]
25	B1732-07	325	8.55 ± 0.07	-0.69 ± 0.05	—	—	—	—	—	—	[1]
		610	5.8 ± 0.1	—	—	—	—	—	—	—	[1]
		1400	3.00 ± 0.08	—	—	—	—	—	—	—	[2]
26	B1737+13	325	1.887 ± 0.009	-0.78 ± 0.09	6.17 ± 0.05	-1.12 ± 0.13	2.78 ± 0.01	-0.78 ± 0.11	0.450 ± 0.005	0.27 ± 0.07	[1]
		408	1.57 ± 0.06	—	4.5 ± 0.3	—	2.4 ± 0.1	—	0.54 ± 0.04	—	[4]
		610	0.977 ± 0.003	—	2.77 ± 0.01	—	1.551 ± 0.006	—	0.560 ± 0.003	—	[1]
		910	0.89 ± 0.04	—	2.2 ± 0.1	—	1.36 ± 0.06	—	0.62 ± 0.04	—	[1]
		1418	0.645 ± 0.001	—	1.780 ± 0.006	—	1.013 ± 0.003	—	0.569 ± 0.002	—	[17]
27	B1738-08	325	—	—	—	—	—	—	1.206 ± 0.009	0.36 ± 0.02	[1]
		610	—	—	—	—	—	—	1.52 ± 0.01	—	[1]
28	B1758-29	325	1.65 ± 0.02	-0.89 ± 0.05	—	—	—	—	—	—	[1]
		610	0.91 ± 0.02	—	—	—	—	—	—	—	[1]
		1400	0.48 ± 0.01	—	—	—	—	—	—	—	[2]
29	B1804-08	610	1.67 ± 0.01	-0.87 ± 0.12	—	—	—	—	—	—	[1]
		925	1.32 ± 0.02	—	—	—	—	—	—	—	[4]
		1400	0.757 ± 0.001	—	—	—	—	—	—	—	[2]
		3100	0.399 ± 0.008	—	—	—	—	—	—	—	[11]
30	B1821+05	325	5.64 ± 0.04	-1.55 ± 0.10	—	—	—	—	—	—	[1]
		408	4.2 ± 0.2	(325–925)	—	—	—	—	—	—	[4]
		610	2.05 ± 0.04	—	—	—	—	—	—	—	[1]
		925	1.11 ± 0.03	—	—	—	—	—	—	—	[4]
		1408	0.98 ± 0.01	—	—	—	—	—	—	—	[4]
31	B1826-17	1642	0.87 ± 0.04	—	—	—	—	—	—	—	[4]
		4850	0.450 ± 0.006	—	—	—	—	—	—	—	[10]
31	B1826-17	925	1.12 ± 0.02	-1.98 ± 0.04	—	—	—	—	—	—	[4]

Table 3 continued on next page

Table 3 (continued)

PSR	Type	Freq (MHz)	S_{score}/S_{score}	$\Delta\alpha$	S_{score}/S_{in}	$\Delta\alpha$	S_{score}/S_{out}	$\Delta\alpha$	S_{in}/S_{out}	$\Delta\alpha$	Ref.
		1408	0.490 ± 0.002	—	—	—	—	—	—	—	[4]
32	B1831-03	925 1400	6.6 ± 0.5 4.8 ± 0.3	-0.74 ± 0.25	—	—	—	—	—	—	[4] [8]
33	B1831-04	325 610	2.60 ± 0.02 1.57 ± 0.01	-0.80 ± 0.02	3.19 ± 0.04 1.48 ± 0.01	-1.22 ± 0.02	2.40 ± 0.02 1.63 ± 0.01	-0.62 ± 0.02	0.75 ± 0.01 1.10 ± 0.01	0.60 ± 0.03	[1] [1]
34	B1839+09	130 170 325 4850	3.6 ± 0.2 3.0 ± 0.1 2.17 ± 0.07 0.89 ± 0.06	-0.56 ± 0.07 (130-325)	—	—	—	—	—	—	[9] [9] [1] [10]
35	B1857-26	325 410 610 925 1400	1.016 ± 0.003 0.786 ± 0.007 0.522 ± 0.002 0.320 ± 0.003 0.283 ± 0.001	-1.00 ± 0.07	3.09 ± 0.01 2.23 ± 0.03 1.154 ± 0.005 0.766 ± 0.009	-1.44 ± 0.09	1.566 ± 0.005 1.15 ± 0.01 0.967 ± 0.005 0.528 ± 0.006	-0.92 ± 0.16	0.507 ± 0.002 0.564 ± 0.007 0.786 ± 0.004 0.690 ± 0.008	0.35 ± 0.20	[1] [4] [1] [4] [2]
36	B1859+03	925 1418 1642	9.8 ± 1.0 4.6 ± 0.2 3.9 ± 0.3	-1.69 ± 0.10	—	—	—	—	—	—	[4] [17] [4]
37	B1907-03	610 1420	7.3 ± 0.5 2.75 ± 0.06	-1.16 ± 0.08	—	—	—	—	—	—	[4] [8]
38	B1907+00	610 1418	11.6 ± 0.6 3.6 ± 0.2	-1.38 ± 0.10	—	—	—	—	—	—	[4] [17]
39	B1907+10	610 1400	13.7 ± 1.4 3.9 ± 0.3	-1.52 ± 0.15	—	—	—	—	—	—	[1] [2]
40	B1911+13	606 1418	5.1 ± 0.4 3.9 ± 0.3	-0.32 ± 0.14	—	—	—	—	—	—	[4] [17]

Table 3 continued on next page

Table 3 (continued)

PSR	Type	Freq (MHz)	S_{core}/S_{cone}	$\Delta\alpha$	S_{core}/S_{in}	$\Delta\alpha$	S_{core}/S_{out}	$\Delta\alpha$	S_{in}/S_{out}	$\Delta\alpha$	Ref.
41 B1914+09	$T_{1/2}$	325	2.93 ± 0.07	-0.78 ± 0.11	—	—	—	—	—	—	[1]
		410	3.0 ± 0.2	—	—	—	—	—	—	—	[4]
		610	1.84 ± 0.06	—	—	—	—	—	—	—	[1]
		925	1.3 ± 0.1	—	—	—	—	—	—	—	[4]
		1400	1.11 ± 0.04	—	—	—	—	—	—	—	[2]
		1642	0.78 ± 0.07	—	—	—	—	—	—	—	[4]
42 B1917+00	T	325	1.86 ± 0.01	-0.57 ± 0.07	—	—	—	—	—	—	[1]
		408	1.69 ± 0.09	—	—	—	—	—	—	—	[4]
		610	1.29 ± 0.02	—	—	—	—	—	—	—	[1]
		1418	1.38 ± 0.05	—	—	—	—	—	—	—	[17]
		1642	1.46 ± 0.12	—	—	—	—	—	—	—	[4]
		—	—	—	—	—	—	—	—	—	—
43 B1918+26	$T_{1/2}$	170	2.07 ± 0.08	-0.28 ± 0.03	—	—	—	—	—	—	[9]
		1418	1.14 ± 0.07	—	—	—	—	—	—	—	[17]
44 B1920+21	$T_{1/2}$	610	6.3 ± 0.2	-1.03 ± 0.21	—	—	—	—	—	—	[4]
		925	3.4 ± 0.8	—	—	—	—	—	—	—	[4]
		1418	2.4 ± 0.3	—	—	—	—	—	—	—	[17]
		1642	2.7 ± 0.3	—	—	—	—	—	—	—	[4]
45 B1929+10	T	120	2.31 ± 0.06	-0.178 ± 0.004	—	—	—	—	—	—	[9]
		140	2.27 ± 0.05	(120–4750)	—	—	—	—	—	—	[9]
		180	2.15 ± 0.04	—	—	—	—	—	—	—	[9]
		325	1.920 ± 0.004	—	—	—	—	—	—	—	[1]
		410	1.83 ± 0.03	—	—	—	—	—	—	—	[19]
		610	1.68 ± 0.01	—	—	—	—	—	—	—	[19]
		925	1.60 ± 0.01	—	—	—	—	—	—	—	[4]
46 B1946+35	T	1710	1.480 ± 0.006	—	—	—	—	—	—	—	[4]
		4750	1.21 ± 0.02	—	—	—	—	—	—	—	[5]
		10550	1.23 ± 0.04	—	—	—	—	—	—	—	[10]
925	8.1 \pm 0.3	-1.53 ± 0.08	—	—	—	—	—	—	—	[4]	

Table 3 continued on next page

Table 3 (continued)

PSR	Type	Freq (MHz)	S_{score}/S_{cone}	$\Delta\alpha$	S_{score}/S_{in}	$\Delta\alpha$	S_{score}/S_{out}	$\Delta\alpha$	S_{in}/S_{out}	$\Delta\alpha$	Ref.
		1418	4.5 ± 0.1	—	—	—	—	—	—	—	[17]
		1642	3.4 ± 0.1	—	—	—	—	—	—	—	[4]
		4850	0.60 ± 0.08	—	—	—	—	—	—	—	[5]
47	B1952+29	610	1.51 ± 0.07	-1.91 ± 0.06	—	—	—	—	—	—	[4]
		1418	0.30 ± 0.01	—	—	—	—	—	—	—	[17]
48	B2002+31	610	16.7 ± 1.0	-1.49 ± 0.11	—	—	—	—	—	—	[4]
		1418	5.15 ± 0.09	—	—	—	—	—	—	—	[17]
		1642	3.4 ± 0.2	—	—	—	—	—	—	—	[4]
49	B2045-16	325	1.069 ± 0.001	-0.53 ± 0.06	—	—	—	—	—	—	[1]
		408	1.124 ± 0.009	—	—	—	—	—	—	—	[4]
		610	0.822 ± 0.001	—	—	—	—	—	—	—	[1]
		925	0.70 ± 0.01	—	—	—	—	—	—	—	[4]
		1400	0.514 ± 0.001	—	—	—	—	—	—	—	[2]
		1642	0.524 ± 0.002	—	—	—	—	—	—	—	[4]
		4850	0.207 ± 0.007	—	—	—	—	—	—	—	[5]
50	B2111+46	408	3.54 ± 0.04	-0.83 ± 0.03	—	—	—	—	—	—	[4]
		610	2.205 ± 0.008	—	—	—	—	—	—	—	[4]
		800	1.57 ± 0.01	—	—	—	—	—	—	—	[16]
		925	1.66 ± 0.02	—	—	—	—	—	—	—	[4]
		1408	1.128 ± 0.003	—	—	—	—	—	—	—	[4]
		1642	1.03 ± 0.01	—	—	—	—	—	—	—	[4]
		4850	0.396 ± 0.002	—	—	—	—	—	—	—	[10]
51	B2210+29	130	0.79 ± 0.03	-0.31 ± 0.04	—	—	—	—	—	—	[9]
		170	0.69 ± 0.02	(130-610)	—	—	—	—	—	—	[9]
		610	0.48 ± 0.01	—	—	—	—	—	—	—	[4]
		1418	0.466 ± 0.006	—	—	—	—	—	—	—	[17]
52	B2224+65	325	4.9 ± 0.4	-1.01 ± 0.11	—	—	—	—	—	—	[7]
		400	2.2 ± 0.3	—	—	—	—	—	—	—	[16]

Table 3 continued on next page

Table 3 (continued)

PSR	Type	Freq (MHz)	S_{core}/S_{cone}	$\Delta\alpha$	S_{core}/S_{in}	$\Delta\alpha$	S_{core}/S_{out}	$\Delta\alpha$	S_{in}/S_{out}	$\Delta\alpha$	Ref.
		610	1.65 ± 0.06	—	—	—	—	—	—	—	[4]
		800	1.22 ± 0.06	—	—	—	—	—	—	—	[16]
		925	0.9 ± 0.1	—	—	—	—	—	—	—	[4]
		1408	0.71 ± 0.03	—	—	—	—	—	—	—	[4]
		1642	0.75 ± 0.06	—	—	—	—	—	—	—	[4]
53	B2327-20	T	1.686 ± 0.003	-0.581 ± 0.008	—	—	—	—	—	—	[1]
		610	1.170 ± 0.005	—	—	—	—	—	—	—	[1]

NOTE— [1]-Mitra et al. (2016); [2]-Johnston & Kerr (2018); [3]-Pilia et al. (2016); [4]-Gould & Lyne (1998); [5]-von Hoensbroech & Xilouris (1997); [6]-Kramer et al. (1997); [7]-Mitra & Rankin (2011); [8]-Seiradakis et al. (1995); [9]-Bilous et al. (2016); [10]-Kijak et al. (1998); [11]-Karastergiou & Johnston (2006); [12]-D'Amico et al. (1998); [13]-Johnston et al. (2006); [14]-Lorimer et al. (1995); [15]-Basu et al. (2020b); [16]-Arzoumanian et al. (1994); [17]-Weisberg et al. (1999); [18]-Wu et al. (1993); [19]-Stairs et al. (1999)